

ARTICLE

Lower troponin expression in the right ventricle of rats explains interventricular differences in E-C coupling

Young Keul Jeon^{1*}, Jae Won Kwon^{1*}, Jihyun Jang^{1,2}, Seong Woo Choi^{3,4}, Joohan Woo³, Su Han Cho¹, Byeong Il Yu¹, Yang Sook Chun^{1,4}, Jae Boum Youm⁵, Yin Hua Zhang^{1,6,7}, and Sung Joon Kim^{1,4,8}

Despite distinctive functional and anatomic differences, a precise understanding of the cardiac interventricular differences in excitation–contraction (E–C) coupling mechanisms is still lacking. Here, we directly compared rat right and left cardiomyocytes (RVCM and LVCM). Whole-cell patch clamp, the IonOptix system, and fura-2 fluorimetry were used to measure electrical properties (action potential and ionic currents), single-cell contractility, and cytosolic Ca^{2+} ($[Ca^{2+}]_i$), respectively. Myofilament proteins were analyzed by immunoblotting. RVCM showed significantly shorter action potential duration (APD) and higher density of transient outward K⁺ current (I_{to}). However, the triggered $[Ca^{2+}]_i$ change (Ca^{2+} transient) was not different, while the decay rate of the Ca^{2+} transient was slower in RVCM. Although the relaxation speed was also slower, the sarcomere shortening amplitude (Δ SL) was smaller in RVCM. SERCA activity was \sim 60% lower in RVCM, which is partly responsible for the slower decay of the Ca^{2+} transient. Immunoblot analysis revealed lower expression of the cardiac troponin complex (cTn) in RVCM, implying a smaller Ca^{2+} buffering capacity (K_S), which was proved by in situ analysis. The introduction of these new levels of cTn, I_{to} , and SERCA into a mathematical model of rat LVCM reproduced the similar Ca^{2+} transient, slower Ca^{2+} decay, shorter APD, and smaller Δ SL of RVCM. Taken together, these data show reduced expression of cTn proteins in the RVCM, which provides an explanation for the interventricular difference in the E–C coupling kinetics.

Introduction

The right ventricle (RV) propels blood into the pulmonary circulation, where the hydraulic impedance is significantly lower than that of the systemic circulation. Consequently, despite the same amount of cardiac output from the two ventricles, the thickness of the RV free wall is lower than that of the left ventricle (LV). As a whole, the RV uses approximately one-fifth of the energy of the LV (Friedberg and Redington, 2014; Foschi et al., 2017). In terms of the work of cardiac cycle, the pressure-volume relationship (P-V loop) of the RV is described as a triangular or trapezoidal shape, with a short isometric period (Redington et al., 1988), different from the square shape in the LV.

The contractile properties of isolated cardiomyocytes from LV (LVCM) and RV (RVCM) have rarely been investigated, while demonstrating variable results in sarcomere length (SL) changes

depending on the animal species and research conditions. A study of mice showed significantly smaller shortening of SL (Δ SL) in RVCM than in endocardial LVCM (Kondo et al., 2006). In rats, the analysis of SL changes revealed the tendency of slower kinetics in RVCM (Carneiro-Júnior et al., 2013). In contrast, canine RVCM showed no significant difference from LVCM in basal SL and Δ SL (Carneiro-Júnior et al., 2013; Molina et al., 2014).

Previous studies of the interventricular differences in the rodent cardiac action potential duration (APD) showed shorter APD in RVCM than LVCM (Watanabe et al., 1983; Knollmann et al., 2001). In addition, canine RVCM showed a deeper notch of phase I in their action potential (AP) than LVCM (Di Diego et al., 1996). Consistent with the shorter APD, the peak amplitudes of cytosolic Ca²⁺ concentration changes triggered by a

¹Department of Physiology, Ischemic/Hypoxic Disease Institute, Seoul National University College of Medicine, Seoul, Republic of Korea; ²Department of Surgery, Center for Vascular and Inflammatory Disease, University of Maryland School of Medicine, Baltimore, MD; ³Department of Physiology and Ion Channel Disease Research Center, Dongguk University College of Medicine, Seoul, Republic of Korea; ⁴Ischemic/Hypoxic Disease Institute, Seoul National University College of Medicine, Seoul, Republic of Korea; ⁵Cardiovascular and Metabolic Disease Center, Department of Physiology, College of Medicine, Inje University, Busan, Republic of Korea; ⁶Yanbian University Hospital, Yanji, China; ⁷Institute of Cardiovascular Sciences, Faculty of Biology, Medicine and Health Sciences, University of Manchester, Manchester, UK; ⁸Wide River Institute of Immunology, Seoul National University College of Medicine, Hongcheon, Republic of Korea.

*Y.K. Jeon and J.W. Kwon contributed equally to this paper; Correspondence to Sung Joon Kim: sjoonkim@snu.ac.kr; Yin Hua Zhang: yinzhang@snu.ac.kr.

© 2022 Jeon et al. This article is distributed under the terms of an Attribution–Noncommercial–Share Alike–No Mirror Sites license for the first six months after the publication date (see http://www.rupress.org/terms/). After six months it is available under a Creative Commons License (Attribution–Noncommercial–Share Alike 4.0 International license, as described at https://creativecommons.org/licenses/by-nc-sa/4.0/).





List of abbreviations

α, parameter describing the series elastic element

 β , parameter describing the series elastic element

 A_p , parameter describing the bridge force of the power work state

 A_{w} parameter describing the bridge force of the weak state

 B_{w} , parameter describing equivalent cross-bridge (CB) kinetics in the weak state

 B_{p} parameter describing equivalent CB kinetics in the power state

CB, attached cross-bridge

f, kinetic reaction function for the CB attaching step

F_b, total CB force

 F_p , parallel force

 F_s , series elastic force

G, parameter representing CB detachment step from TSCa₃~

 G_{dr} parameter representing CB detachment step from TS~

 h_n mean elongation of attached CBs in the power work state

 h_{w} , mean elongation of attached CBs in the weak state

 h_{pr} steady elongation of attached CBs in the power work state

 h_{wr} , steady elongation of attached CBs in the weak state

 J_{trpn} , Ca²⁺ flux toward the myofilaments

 K_e , parameter describing the parallel elastic element

L, half sarcomere length

 L_0 , parameter describing the parallel elastic element

 L_a , parameter constraining the [TSCa₃~]

 L_c , parameter describing the effect of L on g_d

 L_{m} , parameter describing the parallel elastic element

R, parameter constraining the [TSCa₃]

TS, troponin system formed by three troponin-tropomyosin regulatory units

TSCa₃, TS bound to three Ca²⁺

TSCa₃ \sim , TS bound to three Ca²⁺ with three attached CBs in the weak state

TSCa₃*, TS bound to three Ca²⁺ with three attached CBs in the power state

 TS^* , TS without Ca^{2+} with three attached CBs in the power state

TSt, total TS

 X_p , nonelastic portion of the contractile element equal to $L - h_p$

 X_{w_l} nonelastic portion of the contractile element equal to $L - h_w$

 Y_{av} kinetic reaction constant for the CB attaching step

 Y_b , kinetic reaction constant for the binding Ca²⁺ step

 Y_{cl} parameter describing the effect of L on q_{dl}

 Y_d , parameter describing the effect of L on g_d

 Y_{py} Ca²⁺ kinetic reaction constant

Y_a, Ca²⁺ kinetic reaction constant

Y_n Ca²⁺ kinetic reaction constant

Y_ν, Ca²⁺ kinetic reaction constant

 $Z_{a\prime}$ kinetic reaction constant for the CB detaching step

 Z_p , Ca^{2+} kinetic reaction constant

 Z_r , Ca^{2+} kinetic reaction constant

single AP (change in intracellular Ca^{2+} concentration $[\Delta[Ca^{2+}]_i]$ or Ca^{2+} transient) were lower in the RVCM than in the endocardial LVCM of mice (Kondo et al., 2006). However, in rat cardiomyocytes, the $\Delta[Ca^{2+}]_i$ was not different between the RV and LV (Sathish et al., 2006; Carneiro-Júnior et al., 2013).

In addition to the upstroke amplitude, the decay kinetics of the Ca²⁺ transient determine the contractile properties of cardiomyocytes. In an early study of rat RVCM, slower decay of Ca²⁺ transient was observed along with the experimental evidence suggesting a slower rate of Ca²⁺ sequestration by the sarcoplasmic reticulum Ca²⁺-ATPase (SERCA). However, in more recent studies of rodent hearts, the decay of Ca²⁺ transient in RVCM was not different from that in LVCM (Carneiro-Júnior et al., 2013; Molina et al., 2014). The controversial results from previous studies suggested that another Ca²⁺ buffering component, such as Ca²⁺ binding troponin C (TnC), might be different between RVCM and LVCM.

In cardiac myocytes, Ca²⁺ regulates contraction by binding to the thin filament regulatory protein TnC. Along with TnC, the troponin complex (cTn) comprises TnI, which prevents the interaction between myosin and actin filaments, and TnT, which links the TnI-TnC complex to tropomyosin in the thin filament. Ca2+ binding with TnC causes a conformational shift in TnI and TnT, allowing myosin to bind to actin (Sweeney and Hammers, 2018). In addition to the regulation of contraction, Ca²⁺-binding TnC could also contribute to the cytosolic Ca²⁺ buffering capacity (κ_S) of cardiomyocytes. However, the comparison of myofilament expression between RV and LV cardiomyocytes is very rare, let alone the expression of TnC. A recent study of isolated myosin molecules suggested that the mechanical characteristics of working myosin (kinetic rates and the distribution of spatial orientation of myosin lever arm) were the same in both ventricles (Duggal et al., 2017). However, there have been few reports comparing the expression of myofilament components between the two ventricles except 2-D electrophoresis data from porcine and human heart tissues (Phillips et al., 2011; Su et al., 2015).

In this study, we aimed to elucidate the functional differences in excitation-contraction (E-C) coupling along with the expression of myofilament proteins between RVCM and LVCM from rats, focusing on (1) the AP shapes and relevant ionic currents, (2) AP-triggered Ca2+ transients with contraction-relaxation kinetics, (3) the expression of Ca²⁺binding TnC and other cTn proteins, and (4) the Ca²⁺ buffering capacity and Ca2+ sequestration rate by the SR. The results demonstrate intriguing discordant properties between the levels of E-C coupling (APD, $\Delta[Ca^{2+}]_i$, and ΔSL) in terms of biventricular differences. The immunoblot assay revealed lower expression of cTn; in addition, rigorous in situ analysis revealed a lower κ_S , consistent with the lower TnC in RVCM. The SERCA activity was found to be lower in RVCM, consistent with the slower decay rate of the Ca2+ transient. The novel findings regarding cTn and cytosolic κ_S in RVCM could explain the biventricular gaps between the APD, $\Delta[Ca^{2+}]_i$ amplitude, and ΔSL , which were successfully simulated by using a computational model of rodent cardiomyocytes.

3 of 23



Materials and methods

Isolation of ventricular cardiomyocytes

Ventricular cardiomyocytes from Sprague-Dawley rats (RRID: RGD_1566457) were used. The study protocol followed the Guide for the Care and Use of Laboratory Animals published by the US National Institutes of Health (Publication No. 85-23, revised 1996) and also conformed to the Institutional Animal Care and Use Committee of Seoul National University (approval no. SNU-160128-1). 46 male rats were used. At the time of the experiments, the rats were 12 wk old and had mean (\pm SD) body weight of 348.4 \pm 4.68 g.

Cardiomyocytes were isolated using a standard enzymatic dispersion technique, as described previously (Jin et al., 2012), with minor modifications. Briefly, rats were anesthetized with a mixture of ketamine (90 mg · kg⁻¹, i.p.) and xylazine (10 mg · kg-1, i.p.). After monitoring the anesthesia depth with a toe pinch, the hearts were extracted and rapidly mounted onto the Langendorff apparatus at 37°C. Cells were dissociated by a protocol consisting of a constant-flow perfusion (8-10 ml \cdot min⁻¹) for (1) 8 min with Ca²⁺-free Tyrode solution; (2) 8 min with Ca²⁺free Tyrode solution containing enzyme (collagenase 1 mg \cdot ml⁻¹ [Worthington Biochemical Co.], protease, 0.133 mg · ml⁻¹, BSA 1.65 mg \cdot ml⁻¹, and Ca²⁺ 0.05 mM); and (3) a further 10-min digestion period with collagenase-containing Tyrode's solution. In this study, the septum between the two ventricles was not used. Cardiomyocytes were separately harvested from both ventricles and resuspended in cardioplegic storage solution (for IonOptix, in mM; 120 NaCl, 5.4 KCl, 10 HEPES, 5 MgSO₄, 5 Napyruvate, 5.5 glucose, 20 taurine, 29 mannitol, and 0.2 CaCl₂, pH 7.4) or Kraft-Brühe (K-B) solution (for electrophysiology, in mM; 50 L-glutamate, 70 KOH, 55 KCl, 10 HEPES, 0.5 EGTA, 20 KH₂PO₄, 20 taurine, 20 glucose, and 3 MgCl₂, pH 7.3). The proportion of rod-shaped cardiomyocytes ranged from 60 to 80%. Cardiomyocytes for physiological assays were used immediately, and cardiomyocytes for biochemical assays were centrifuged and stored at -80°C.

Electrophysiology

Freshly isolated cardiomyocytes were transferred into a bath mounted on the stage of an inverted microscope (Ti; Nikon). The bath (0.15 ml) was continuously perfused at a constant rate (5 ml · min⁻¹), and voltage-clamp experiments were performed at room temperature (22-25°C). Borosilicated glass pipettes with a free-tip resistance of ${\sim}2.5~\text{M}\Omega$ were used for whole-cell and perforated whole-cell patch clamp. The series resistance, estimated by dividing the time constants of the capacitive current, was kept <10 MΩ in the whole-cell configuration and <16 MΩ in the perforated whole-cell configuration. To correct for cell size, the absolute current amplitudes were divided by the cell capacitance and expressed as $pA \cdot pF^{-1}$. The pipettes were connected to the CV 203BU head stage of the Axopatch 200B, a patch-clamp amplifier (Molecular Devices). pCLAMP software v10.6.2 and Digidata-1440A (Molecular Devices) were used to acquire data and apply command pulses. The recorded currents were sampled at 10 kHz and low-pass Bessel filtered at 5 kHz. The recorded data were processed using Clampfit v11.0.1 (Molecular Devices).

Single cardiomyocyte contraction and $\Delta[Ca^{2+}]_i$ measurements using the lonOptix system

The physiological properties of cardiomyocytes were measured using the IonOptix system (IonOptix). The contractility was measured by detecting the length of two edges with a contractility recording system at a 2-6-Hz frequency of field stimulation. Soft-edge software (IonOptix) was used to capture and analyze the changes in SL, and the results were given as fractional shortening. For [Ca²⁺], measurement, cardiomyocytes were incubated with 2 µM fura-2-acetoxymethyl ester (fura-2-AM) for 15 min at room temperature. After sedimentation, the supernatant was removed, and cardiomyocytes were reintroduced into a perfusion solution containing 500 µM Ca²⁺ for 10 min. Then, the fura-2-AM-loaded cardiomyocytes were placed in a bath and excited by 360- and 380-nm filtered fluorescent light. The emitted signal was measured simultaneously with photomultiplier tubes. [Ca2+]i was calculated using the in situ calibration described below and the estimated dissociation constant (K_d) of fura-2-AM $(K_{d,fura-2})$. Measurements from ≥20 steady-state contractions were averaged for each cardiomyocyte for each stage of the experimental protocol. All experiments were performed in a temperature-controlled bath solution at 37 ± 1°C.

Isolation of membrane/cytosol fraction and myofilament fraction

The sampling for Western blotting (immunoblotting) was performed in two different ways, as described previously (Jang et al., 2015). The membrane/cytosol fraction was extracted from cardiomyocytes using lysis buffer containing 0.5 mM EGTA, 25 mM Tris-HCl, 150 mM NaCl, and 1% Triton X-100 with phosphatase and protease inhibitor cocktail (Roche) following centrifugation. To obtain the myofilament fraction, cardiomyocytes were washed with cold PBS and transferred to screw-cap tubes containing 2.5 mm zirconia/silica beads and cold buffer (60 mM KCl, 30 mM imidazole, 2 mM MgCl₂, and 1% Triton X-100 with protease and phosphatase inhibitor cocktail). The cells in the lysis buffer were homogenized with a bead beater (Mini-Beadbeater-8; BioSpec Products) for 20 s, and the homogenates were centrifuged at 8,000 rpm for 10 min at 4°C. The supernatant was discarded, and the process was repeated at least six times. The remaining pellets (myofilament-enriched fraction) were resuspended in the high-salt buffer (Bio-Rad) and used in subsequent experiments.

Immunoblotting

Lysates were quantified using the Bradford method (Bio-Rad) and heated at 95°C for 5 min. Lysates were fractionated by SDS-PAGE and transferred to PVDF membranes (Bio-Rad) in 25 mM Tris, 192 mM glycine, 0.01% SDS, and 20% methanol. Membranes were blocked in 1× TBS containing 1% Tween-20 and 5% BSA (blocking solution) for 1 h at room temperature with gentle rocking. Membranes were then incubated overnight at 4°C with TnC (RRID:AB_306435; Abcam), TnI (RRID:AB_2206278; Cell Signaling), TnT (RRID:AB_261723; Sigma-Aldrich), tropomyosin (RRID:AB_261817; Sigma-Aldrich), desmin (RRID:AB_306653; Abcam), actinin (RRID:AB_476766; Sigma-Aldrich), and α -actin



Table 1. Solutions used in the present study (in mM)

	NT	0 Na/0 Ca	0 Na/2 Ca	AP-pipette	VOCC _L -pipette	K-pipette	Cs-pipette	Ca ²⁺ -calibration
NaCl	141.4	141.4				5		
LiCl			141.4					
CsCl					140		140	
KCl	4	4	4	140		25		140
K-Asp						115		
HEPES	10	10	10	10	10	10	10	10
EGTA				0.1	0.1	10		10
NaH ₂ PO ₄	0.33	0.33						
MgATP						4	4	
MgCl ₂	1	5	1			1	1	1
CaCl ₂	1.8		2					-
Glucose	5.5	5.5	5.5					
рН	7.4	7.4	7.4	7.2	7.2	7.2	7.2	7.2

(RRID:AB_476695; Sigma-Aldrich) primary antibodies, SERCA2a (Abcam), phospholamban (RRID:AB_2617049; Badrilla), and phosphor-PLB (RRID:AB_310352; Millipore) followed by secondary antibodies after washing. Blots were developed using ECL Plus Western blotting detection reagents (Merck). The relative densities were calculated by normalizing each blot to actin. The number of experiments means each different animal. We excluded the results that showed large differences in internal control (10%) between LV and RV protein samples.

In situ analysis of the Ca2+ binding ratio and Ca2+ removal

For these experiments, a whole-cell patch clamp was conducted with simultaneous fura-2 fluorescence ratiometry (PTI). The Cspipette solution contained 50 μ M fura-2 pentapotassium salt (Table 1, Cs-pipette). Light from a xenon arc was collected and filtered at 340 and 380 nm with 10 nm full width at half-maximum. The filtered light of the region of interest surrounding the cardiomyocyte was passed through the epifluorescence port of the inverted microscope and the CFI Super Fluor objective lens (Nikon). The emitted light was filtered at 510 nm and measured simultaneously using a photomultiplier tube (PTI).

To estimate the endogenous cytosolic buffer components, we defined the endogenous (intrinsic) Ca^{2+} binding ratio (κ_S) in terms of a hypothetical Ca^{2+} binding species "S" (Mathias et al., 1990). The κ_S and Ca^{2+} -binding ratio of the total buffer including fura-2 (κ_B) were defined as follows:

$$[CaB] = [CaS] + [Cafura2];$$

$$\kappa_{S} \equiv \frac{d[\mathsf{CaS}]}{d[\mathsf{Ca}^{2^{+}}]} = \frac{K_{d,S}[\mathsf{S}]_{tot}}{\left(K_{d,S} + \left[\mathsf{Ca}^{2^{+}}\right]\right)^{2}};$$

$$\kappa_{\rm B} = \frac{d[{\rm CaB}]}{d[{\rm Ca}^{2+}]} = \frac{K_{d,\rm B}[{\rm B}]_{\rm tot}}{(K_{d,\rm B} + [{\rm Ca}^{2+}])^2}$$
(2)

where $[S]_{tot}$ is the net concentration of cytosolic Ca²⁺ buffer, $[B]_{tot}$ is the concentration of the total buffer including fura-2, $K_{d,S}$ is the dissociation constant of the cytosolic buffer, and $K_{d,B}$ is the dissociation constant of the total buffer. κ_B was determined by measuring the change in [Ca²⁺]_i and the net amount of calcium influx during depolarization (i.e., the integral of the Ca²⁺ current; see Fig. 7; Berlin et al., 1994). For this purpose, after establishing the whole-cell configuration, the cell was depolarized with a ramp-like pulse from -70 to -40 mV (300 ms) to inactivate the voltage-gated Na+ current, followed by 100 ms of 10-mV depolarization to activate the voltage-operated Ca²⁺ channel (VOCC_L). After confirming the steady-state amplitudes of the Ca²⁺ transient in normal Tyrode (NT), the SERCA inhibitor (2.5 µM thapsigargin) was applied for 5 min, followed by 20 mM caffeine to deplete the SR Ca²⁺ store. In addition, the extracellular solution was changed to a O Ca/O Na solution (Table 1) to inhibit the sodium-calcium exchanger (NCX). Then, Ca²⁺ was added back (0 Na/2 Ca solution; Table 1) with simultaneous depolarization from -40 to 10 mV (200 ms, 1 Hz). To measure the Ca-binding ratio (κ_B), the change in $[Ca^{2+}]_i$ induced by each depolarizing pulse under the above conditions $(d[Ca^{2+}]_i)$ was measured using fura-2 ratiometry at room temperature. The change in bound calcium (d[BCa]) was calculated using Eq. 3:

$$d[BCa] = \Delta[Ca^{2+}]_{tot \ cal} - d[Ca^{2+}]_{i}.$$
 (3)

The mechanisms responsible for Ca^{2+} removal were investigated using Ca^{2+} imaging as described by Díaz et al. (2004). We defined the time constant of decay of $[Ca^{2+}]_i$ as τ_{tran} measured when depolarizing stimulation was applied. In caffeine treatment, the time constant was defined as τ_{caff} that would reflect the Ca^{2+} removal kinetics except for SERCA. The time constant of decay with caffeine in 0 Ca/0 Na solution (τ_{ONaOCa}) was regarded to reflect the Ca^{2+} removal kinetics of plasma membrane Ca^{2+} -ATPase (PMCA) and other slow components. To quantify the relative contribution of Ca^{2+} removal, the reciprocal of the time constant was taken and converted into rate constants (k_{tran} ,



 k_{caff} , and k_{ONaOCa}). In this model, the released Ca²⁺ from SR could be removed by (1) three active components (SERCA, NCX, and PMCA) and (2) endogenous Ca²⁺ buffers. As our present study demonstrated the lower endogenous Ca2+ buffering capacity in RVCM (see Fig. 8), we expected that the amount of Ca²⁺ binding to endogenous Ca²⁺ buffer would be larger in LVCM during the caffeine-induced Ca2+ transient, which also suggested the possibility of underestimating the SERCA activity of LVCM. To correct the error from difference in endogenous buffer, we assumed that total Ca2+ is a linear function of free Ca2+ at the relatively higher range where SERCA activity is measured (dotted line in Fig. 8, G and H). Although the linear relationship was not observed at low free Ca^{2+} concentrations (~300 nM), the concentration of Ca^{2+} transient used for fitting to the exponential function was higher than resting levels, implying that the assumption was reasonable. Given this assumption, the rate constants of three Ca2+ removal machinery was multiplied by the buffer power of each ventricle, which was named "relative rate constant" (see Fig. 4 F).

In vitro K_{d,fura-2} mimicking the cytosolic environment

The properties of fura-2, such as its $K_{d,fura-2}$ value when associated with Ca2+, are known to change in the cytosolic environment due to its binding with proteins (Konishi et al., 1988). Therefore, we conducted an in vitro calibration according to the method described by Berlin et al. (1994). The free Ca²⁺ concentrations of the calibration solutions were calculated with Slider, v2.0 (written by Chris Patton, Pacific Grove, CA), which used the equation from Fabiato and Fabiato (1979). To obtain the $K_{d.fura-2}$ value in the cytosolic environment, we used Ca²⁺-buffered (10 mM EGTA) KCl solution containing 283 mM sucrose or 20 mg/ml aldolase to reflect the viscosity and the fura-2-binding property of cytosolic proteins, respectively (Ca²⁺-calibration solution in Table 1). The viscosity-protein and -sucrose relationships were measured using an Ubbelohde-type viscometer under the assumption of a Newtonian fluid (Fig. S1 A). To minimize the error factor from the depth of the bath solution, a calibration solution constrained between two round coverslips (diameter 18 mm) was used (Fig. S1 B). From the amount of the calibration solution and the size of coverslips, we estimated the distance between the coverslips to be 120-140 μm , which was ~10 times the average thickness of cardiomyocytes, 13 µm (Satoh et al., 1996). To obtain a fluorescence light intensity similar that of fura-2 loaded into cardiomyocytes, the concentration of fura-2 in the in vitro calibration was lowered to 5 μ M. We then measured $K_{d,fura-2}$ in three types of calibration solutions (Fig. S1 C): (1) standard calibration solution (normal), (2) viscositycorrected calibration (sucrose), and (3) protein-containing calibration solution (protein). Because the K_{d,fura-2} values of the standard and viscosity-corrected calibration solutions were significantly lower than those of the protein-containing solutions (Fig. S1 D), we used the K_{d,fura-2} value of the protein-containing calibration, in accordance with previous measurement of Berlin et al. (1994). In this study, the in situ $K_{d,fura-2}$ of fura-2 was 381.8 nM.

In situ calibration of fura-2 fluorescence ratiometry

It is well known that there are several problems in calibrating Ca²⁺ concentration in cardiomyocytes, including hypercontraction of

cells at $[Ca^{2+}]_i > 1 \, \mu M$, which distorts the path length and membrane integrity (Cheung et al., 1989). To overcome this problem, we measured the calibration parameters, R_{\min} , R_{\max} , and β , in separate experiments according to the lanthanum-method described by Borzak et al. (1990). Conversion factors were measured using a cuvette-type spectrophotometer with an identical right source and calculated as $C_1 = R_{\max,Ca}/R_{\max,La}$ and $C_2 = F_{380\max,Ca}/F_{380\max,La}$ (Fig. S2). These La³⁺-derived proportionality constants were determined to convert the fluorescence signal of La³⁺ to that of Ca²⁺.

Determination of fura-2-accessible cytosolic volume and the effective [fura-2] in situ

There is a linear correlation between membrane capacitance (C_m) and total cellular volume (vol_{tc}) , and the ratio C_m/vol_{tc} was 6.76 pF \cdot pl⁻¹ in 12-wk-old adolescent rats (Satoh et al., 1996). Because mitochondria and other organelles occupy ~35% of total cellular volume of cardiomyocytes, we estimated the cytosolic cell volume accessible to fura-2 (vol_{ac}) as 0.65 vol_{tc} (Berlin et al., 1994). Fura-2 dialyzed into the cells could be partly bound to proteins (e.g., myofilaments) while maintaining the Ca²⁺-binding property. Therefore, it is necessary to estimate their effective cytosolic concentration of fura-2. At the end of every experiment, the fluorescence intensity of the cell at the isosbestic wavelength of fura-2 was measured and normalized to the accessible volume (F_{cell}/vol_{ac}) . In addition, the fluorescence of a glass capillary with a 20-µm inner diameter containing 50 µM of fura-2 was measured when placed in the same position as the cell within the region of interest of known length to obtain a standard fluorescence per unit volume ($F_{standard}$) at the isosbestic wavelength. The effective net concentration of fura-2 ([fura2]_{tot}) was calculated as follows:

[fura, 2]_{tot} =
$$F_{cell}/F_{standard}$$
 · 50 μ M · 1/ Φ

where Φ is the ratio of fluorescence intensity in the presence and absence of aldolase at pCa 7.0.

Solution and chemicals

Solutions for electrophysiology, Ca^{2+} measurement, and the IonOptix system are listed in Table 1. We used three external solutions: NT, 0 Na/0 Ca, and 0 Na/2 Ca. Four types of pipette solutions were used depending on the experimental conditions (AP-, VOCC_L-, K-, and Cs-pipette). All drugs and chemicals were obtained from Sigma-Aldrich.

Data presentation and statistics

For analysis of the activation and inactivation kinetics of the current of VOCC_L ($I_{Ca,L}$) and transient outward K^+ current (I_{to}), the conductance was normalized to the maximal conductance and fitted by a Boltzmann equation. The time constants of inactivation, τ , were obtained by fitting the current trace with a dual exponential function. Data are presented as mean \pm SD, with n denoting the number of cells and N denoting the number of animals. Data were compared using a nested t test was where appropriate, taking into account n cells and N animals (Sikkel et al., 2017; Eisner, 2021). Current amplitudes of I_{to} and $I_{Ca,L}$ were



assessed using MANOVA in Origin software (MANOVA app, v1.22). Differences were considered significant when P < 0.05. Asterisks were used in the graphs to indicate significance of statistical inference (*, P < 0.05; **, P < 0.01; ***, P < 0.001; and ****, P < 0.0001). Curve fitting with the least-squares method was performed using Origin (Microcal Software) or handwritten Python software.

Computational simulation of AP

Mathematical models of rat ventricular AP described by the Hodgkin-Huxley-type differential equation were used (Pandit et al., 2001). The model consists of three intracellular compartments: myoplasm, junctional SR, and network. The total ionic current (I_{ion}) is given by

$$I_{ion} = I_{Na} + I_{Ca,L} + I_{to} + I_{ss} + I_{f} + I_{K1} + I_{B} + I_{NaK} + I_{CaP} + I_{NaCa}$$

where I_{Na} is the fast inward Na⁺ current, $I_{Ca,L}$ is the VOCC_L current, I_{to} is the transient outward K⁺ current, I_{ss} is the steady-state outward K⁺ current, I_f is the hyperpolarization-activated funny current, I_{K1} is the inward rectifier K⁺ current, I_B is the background current, I_{NaK} is the Na⁺-K⁺ pump, I_{CaP} is the Ca²⁺ pump, and I_{NaCa} is the NCX.

In the original Pandit model, the I_{to} current is modeled as

$$I_{to} = g_t r(as + bs_{slow})(V - E_K),$$

where g_t is the maximum conductance for I_{to} , r is the activation gating variable, a and b are proportionality coefficients, V is the membrane potential, E_K is the reversal potential of K^+ , and s and s_{slow} represent fast and slow inactivation gating variables, respectively.

Computational simulation of [Ca2+]i and contraction

The Ca²⁺-buffering effect of the troponin system, as represented by I_{tropn} , was used to calculate free cytosolic [Ca²⁺] in the mathematical model of rat ventricular AP (Pandit et al., 2001). We replaced the simple Ca²⁺-buffering troponin model by Pandit et al. (2001) with the cardiac muscle model developed by Negroni and Lascano (2008) to calculate free cytosolic [Ca²⁺] as well as SL and force. Systolic and diastolic [Ca²⁺] by those two models were in the similar range (systolic, 400–600 nM; diastolic, ~100 nM). The model equations are as follows:

$$\begin{split} \frac{d[\text{TSCa}_3]}{dt} &= Y_b[\text{TS}][\text{Ca}^{2+}]^3 - Z_b[\text{TSCa}] + \\ g[\text{TSCa}_3 \sim] - f[\text{TSCa}_3]; \\ \\ \frac{d[\text{TSCa}_3 \sim]}{dt} &= f[\text{TSCa}_3] - g[\text{TSCa}_3 \sim] + \\ Z_p[\text{TSCa}_3^*] - y_p[\text{TSCa}_3 \sim]; \\ \\ \frac{d[\text{TSCa}_3^*]}{dt} &= y_p[\text{TSCa}_3 \sim] - Z_p[\text{TSCa}_3^*] + \\ Z_r[\text{TS}^*][\text{Ca}^{2+}]^3 - y_r[\text{TSCa}_3^*]; \\ \\ \frac{d[\text{TS}^*]}{dt} &= y_r[\text{TSCa}_3^*] - Z_r[\text{TS}^*][\text{Ca}^{2+}]^3 - g_d[\text{TS}^*]; \end{split}$$

$$\begin{split} \left[\text{TS} \right] &= \left[\text{TSt} \right] - \left[\text{TS}^* \right] - \left[\text{TSCa}_3^* \right] - \left[\text{TSCa}_3 \sim \right] - \left[\text{TSCa}_3 \right]; \\ J_{trpn} &= \frac{d \left[\text{Ca}_{trpn} \right]}{dt} = 3 \begin{pmatrix} \frac{d \left[\text{TSCa}_3 \right]}{dt} + \frac{d \left[\text{TSCa}_3 \sim \right]}{dt} + \\ \frac{d \left[\text{TSCa}_3^* \right]}{dt} \end{pmatrix}; \\ f &= y_a e^{-R(L-La)^2}; \\ g &= Z_a + Y_h; \\ Y_h &= \begin{cases} 0.1 \cdot Y_\nu \left[1 - e^{-28,000(h\nu - h\nu r)^2} \right], \ h_\nu - h_{\nu r} < 0 \\ Y_\nu \left[1 - e^{-28,000(h\nu - h\nu r)^2} \right], \ h_\nu - h_{\nu r} \ge 0 \end{cases}; \\ a_1 &= Y_1 e^{-Y_2 (L-Lc)^2} \end{split}$$

SL and force were calculated as

$$\begin{split} \frac{dX_{w}}{dt} &= B_{w} (h_{w} - h_{wr}); \\ \frac{dX_{p}}{dt} &= B_{p} (h_{p} - h_{pr}); \\ h_{w} &= L - X_{w}; \\ h_{p} &= L - X_{p}; \\ F_{b} &= A_{w} \cdot \left[TSCa_{3} \sim \right] \cdot h_{w} + A_{p} \cdot \left(\begin{bmatrix} TSCa_{3}^{*} \end{bmatrix} + \right) \cdot h_{p}; \\ F_{s} &= \alpha \left[e^{\beta(Lm-L)} - 1 \right]; \\ F_{p} &= K_{e} (L - L_{0})^{5} + L_{e} (L - L_{0}) \\ F_{s} &= F_{b} + F_{p}. \end{split}$$

These variables are listed in the List of abbreviations, and the numerical values of the parameters are listed in Table 2. The diagram of the troponin states described by Negroni and Lascano (2008) was used in this study with minor modification (Fig. S3).

Online supplemental material

Fig. S1 shows the methods of in vitro calibration for measuring $K_{d,fura-2}$. Fig. S2 shows the spectra of fura-2-Ca²⁺ and fura-2-La³⁺ and converting factors between two measurements. Fig. S3 shows the diagram of troponin states used in this study. Fig. S4 shows the AP analysis for each animal. Fig. S5 shows the inactivation time constants of I_{to} and $I_{ca,L}$. Fig. S6 shows the Ca²⁺ transient analysis for each animal. Fig. S7 shows the immunoblotting of cTn and tropomyosin while varying the total loading protein amount. Fig. S8 shows the sarcomere shortening analysis for each animal. Fig. S9 shows the changes in sarcomere shortening pattern according to the stimulation frequency. The box-and-whisker plots in Figs. S4, S6, and S8 display the fivenumber summary of a set of data including the minimum, first quartile, median, third quartile, and maximum.

Results

Electrophysiological properties

The APs of RVCM and LVCM were triggered by a 6-ms square pulse (\sim 1.0 nA of current injection, 2 Hz) under the nystatin-perforated mode of current-clamp (Fig. 1 A). In separate experiments under the conventional whole-cell mode, electrical membrane capacitances (C_m) were measured, which showed a



larger C_m in LVCM than in RVCM (Fig. 1 B). All the parameters analyzed in the AP recordings were obtained in the nystatinperforated condition (Fig. 1, C-M). Peak amplitudes, time to reach peak depolarization (peak time), resting membrane potential (RMP), maximum increasing speed, and time of the maximum increasing speed were not different between LVCM and RVCM (Fig. 1, C-G). In contrast, the repolarization was more rapid in RVCM; and higher maximum decreasing speed (Fig. 1 H); shorter time of maximum decreasing speed from the stimulus (MdT) and from the peak time (MdT from peak; Fig. 1, I and J), and shorter APD at 10, 50, and 90% of repolarization (APD₁₀, APD₅₀, APD₉₀) were seen in RVCM than in LVCM (Fig. 1, K and M). Six and five Sprague-Dawley rats were used for measuring capacitance and AP, respectively. The statistical significance between RVCM and LVCM was analyzed by nested t test (Fig. S4).

Because the faster repolarization suggested larger voltagedependent K+ conductance, we measured the K+ currents activated by depolarizing step pulses from -90 mV holding voltage under the conventional whole-cell voltage-clamp. A VOCC_L blocker (nifedipine, 10 µM) was added to the bath solution. Fast activating transient outward currents (Ito) and sustained outward currents were observed (Fig. 2 A). The amplitudes of I_{to} —that is, the inactivating component of outward current were normalized to C_m and plotted against the test voltages (I/V curves; Fig. 2 B). I_{to} was larger in RVCM than LVCM (131 ± 5.8% at 60 mV, P < 0.0001). Voltage-dependent inactivation of I_{to} was analyzed using a two-step voltage-clamp protocol. A common test pulse to 30 mV (200 ms) was applied at the end of the conditioning step (1 s) to different potentials (inset of Fig. 2 C). Inactivation was determined as the ratio of the test current amplitude to the maximum test current. The voltage dependence of inactivation was fitted by a Boltzmann function, providing a half-inactivation voltage $(V_{1/2,inact})$ and slope factor (k). The $V_{1/2,inact}$ and k values were not significantly different between RVCM and LVCM (Fig. 2 C). The kinetics of the inactivating components were further analyzed by fitting to double exponential functions. The time constants for the fast and slow components did not differ between RVCM and LVCM (Fig. S5, A and B).

The current of $VOCC_L$ ($I_{Ca,L}$) generates prolonged depolarization of the cardiac AP, which determines the APD; therefore, we measured the $I_{Ca,L}$ using Cs-pipette solution under the nystatin-perforated patch clamp condition to minimize the decay of $I_{Ca,L}$. Steplike depolarizations from -40 mV holding voltage were applied. Voltage-dependent activation of inward currents with relatively slow inactivation was observed (Fig. 2 D). The peak amplitudes normalized to C_m were plotted against the test voltages, and the I/V curves did not differ between RVCM and LVCM (Fig. 2 E). Steady-state voltage-dependent inactivation was analyzed using a two-step voltage clamp protocol. The pulses were applied to a test potential of 10 mV (300 ms) from various conditioning pulses (-80 mV to 20 mV, 300 ms; inset of Fig. 2 F). The voltage dependence and kinetics of $I_{Ca,L}$ inactivation did not differ between RVCM and LVCM (Fig. 2 F and Fig. S5, C and D).

Table 2. Numerical values of the parameters

Ap	10,080 Mn mm ⁻² μm ⁻¹ μM ⁻¹
$\overline{A_{w}}$	2,016 mN mm ⁻² μm ⁻¹ μM ⁻¹
α	0.5 mN mm ⁻²
β	80 μm ⁻¹
B _w	0.35 ms ⁻¹
B _p	0.5 ms ⁻¹
h _{pr}	0.006 μm
h _{wr}	0.0001 μm
K _e	105,000 mN mm ⁻² μm ⁻⁵
Lo	0.97 μm
L _a	1.15 μm
L _c	1.05 μm
L _m	1.05 μm
R	15 μm ⁻²
[TSt]	23 μΜ
Y _a	0.0023 ms ⁻¹
$\overline{Y_c}$	4.0 ms ⁻¹
Y _b	$0.1816~\mu M^{-3}~ms^{-1}$
$\overline{Y_d}$	0.0333 ms ⁻¹
Y _p	0.1397 ms ⁻¹
Y _r	0.1397 ms ⁻¹
Y _v	0.9 ms ⁻¹
Z _a	0.0023 ms ⁻¹
Z _b	0.1397 ms ⁻¹
Z _p	0.2095 ms ⁻¹
Z _r	7.2626 μM ⁻³ ms ⁻¹

Using a mathematical electrophysiology model of rat ventricular cardiomyocytes (Pandit et al., 2001), we simulated the effects of the higher I_{to} in RVCM (Fig. 2, dotted lines). The Pandit model simulating the cardiac AP of the "left" ventricular AP was modified according to the experimental data of the RV. As the measured parameters representing the kinetics of I_{to} did not differ from those of the Pandit model, we modified only the conductance of I_{to} to reflect the measured values. It was also notable that the $I_{Ca,L}$ of the Pandit model, 7.8 ± 0.2 pA · pF⁻¹ at 10 mV (Katsube et al., 1998), was smaller than our experimental data, 9.0 \pm 0.78 pA \cdot pF⁻¹ at 10 mV (Fig. 2, D and E). Therefore, to reflect this difference, we modified the maximum conductance for $I_{Ca,L}$ ($g_{Ca,L}$ in the original model) in our RVCM and LVCM models. The calculated APD of rat RVCM was shorter than that of LVCM (Fig. 2 G), similar to the experimental data (Fig. 1 A and Table 3).

The amount of net Ca^{2+} influx would also be limited by the shorter APD inducing faster termination of $I_{Ca,L}$. However, the peak amplitude of $I_{Ca,L}$ during the actual AP might not be smaller or could even be larger in RVCM with larger I_{to} , owing to the electrical driving force for the Ca^{2+} influx through the not-yet-deactivated VOCC_L (Harris et al., 2005). Consistent with the



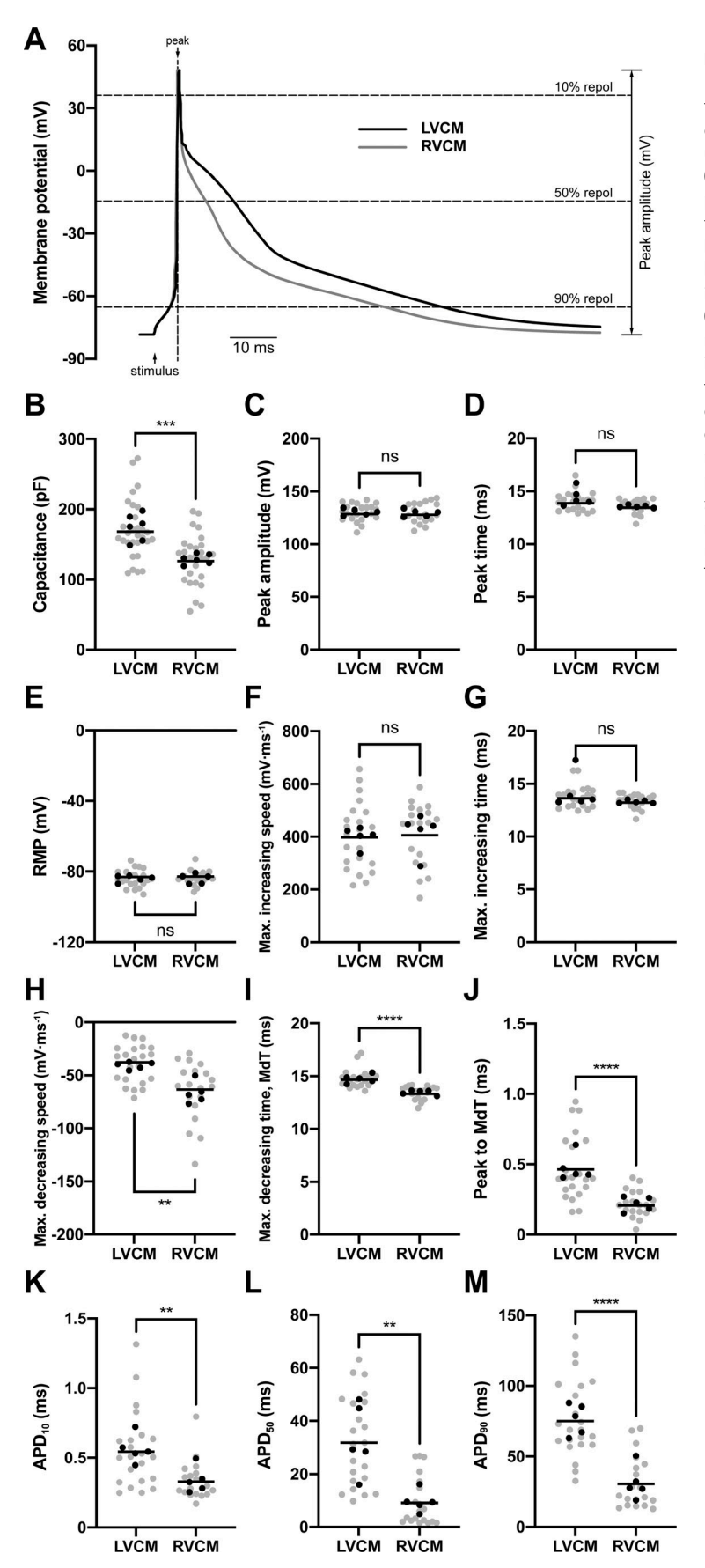


Figure 1. Shorter AP duration with faster repolarization in RVCM. (A) Representative traces of AP in LVCM (black line) and RVCM (gray line). APs were evoked by 6 ms of square pulse under the current-clamp mode of nystatin-perforated whole-cell patch clamp. (B) Membrane capacitance (C_m) separately measured under the conventional whole-cell mode (n = 29 and 27, n = 6). (C-M) Summary of AP parameters measured in the nystatinperforated recordings (n = 22 and 19, n = 5). (C) Peak amplitude; from RMP to peak depolarization. (D) Peak time; time difference between the onset of stimuli and the peak AP (the distance between the two vertical arrows in A). (E) RMP. (F) Maximal increasing speed; the maximum speed of AP depolarization. (G) Maximum increasing time; the time point showing the maximum increasing speed from the onset of stimuli. (H) Maximum decreasing speed; the maximum speed of AP repolarization after the peak. (I) Maximum decreasing time (MdT); the time of MdT from the onset of stimuli. (1) Peak to MdT; the time duration from AP peak to MdT. (K-M) APD₁₀, APD₅₀, and APD₉₀, representing the time to repolarize 10, 50, and 90% from the peak, respectively. All statistical tests performed using nested t test. **, P < 0.01; ***, P < 0.001; ****, P < 0.0001. The gray dot means the measured value of individual cells, and the block dot represents the average of the measured value for each animal. The black line in the column means average of measured value. Repol, repolarization.



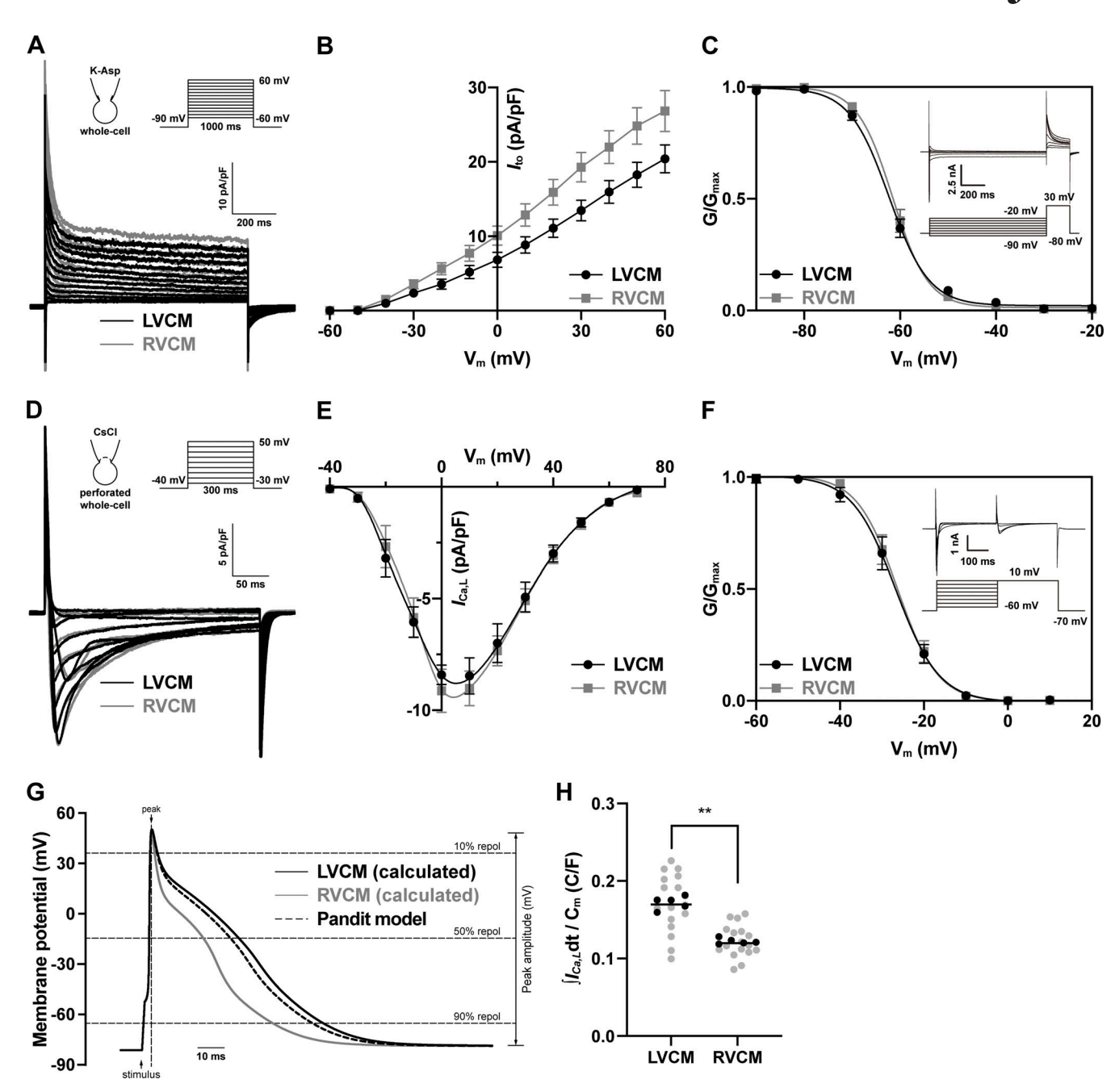


Figure 2. **Electrophysiological comparison between RVCM and LVCM.** (**A–C**) Larger I_{to} in RVCM. (**A**) Representative traces of I_{to} activated by step pulses from -60 to 60 mV (1 s) every 10 s in LVCM (black line) and RVCM (gray line). (**B**) Density of I_{to} (amplitude of fast inactivating outward current/membrane capacitance) plotted against the clamp voltage (n = 23 and 21, n = 6, P < 0.0001). (**C**) Voltage-dependent inactivation curves obtained by a double-pulse protocol (inset) and fitted to the Boltzmann equation. The peak current elicited by the common test pulse (30 mV) was normalized to the maximum value and plotted as a function of the conditioning voltages (-90 to -20 mV). The half-maximum inactivation voltage ($V_{1/2,inact}$) did not differ between RVCM and LVCM. (**D–F)** VOCC_L current ($I_{Co,L}$) and AP-induced Ca²⁺ influx. (**D**) Representative traces of $I_{Co,L}$ recorded under the nystatin-perforated patch clamp using CsCl pipette solution. $I_{Co,L}$ was activated by repetitive step pulses from -30 to 50 mV (300 ms) every 10 s. The presented traces are nifedipine-sensitive currents in LVCM (black line) and RVCM (gray line). (**E**) The peak amplitudes of the nifedipine-sensitive current were normalized to C_m and plotted against the test voltage (n = 22 and 19, n = 6). (**F**) Steady-state voltage-dependent inactivation of $I_{Co,L}$ was obtained by two-step pulse protocol (inset). The evoked pulse at 10 mV (300 ms) from various conditioning pulses normalized to the maximum value and plotted as a function of the conditioning potential. The G-V relationships were fitted to the Boltzmann function, showing no difference between the two ventricles. We tested the significance of I_{to} and $I_{Co,L}$ using MANOVA. (**G**) Mathematical simulation of AP. The calculated APs of the Pandit model (Pandit et al., 2001; dotted line) and the modified results reflecting the measured parameters in LVCM (black solid line) and RVCM (gray line). (**H**) Summary of



Table 3. Comparison between the recorded and calculated AP of two ventricles (Pandit et al., 2001)

	Recorded AP	Calculated AP					
Parameter	LVCM	RVCM	Ratio	Pandit	LVCM	RVCM	Ratio
Peak amplitude (mV)	129.7 ± 3.72	128.5 ± 2.88	0.99	132.8	132.9	130.7	1.01
RMP (mV)	-83.8 ± 1.04	-83.7 ± 0.91	1.00	-84.1	-84.1	-84.0	1.00
APD ₅₀ (ms)	32.9 ± 4.17	15.7 ± 3.72	0.47	30.8	34.0	20.8	0.61
APD ₉₀ (ms)	70.0 ± 5.46	45.1 ± 6.74	0.64	65.2	69.4	50.3	0.72

latter possibility, it has been reported that a loss of the notch due to reduction of I_{to} contributes to the reduced Ca^{2+} influx in failing hearts of larger mammals (Cooper et al., 2010). To elucidate the actual Ca^{2+} influx via $VOCC_{L}$, we compared the $I_{Ca,L}$

induced by the AP-clamp protocol in RVCM and LVCM. In fact, the peak amplitude of inward $I_{Ca,L}$ became higher, and the decay became faster, when applying the RVCM-type versus the LVCM-type AP clamp. Overall, the cumulative Ca^{2+} influx—that is,

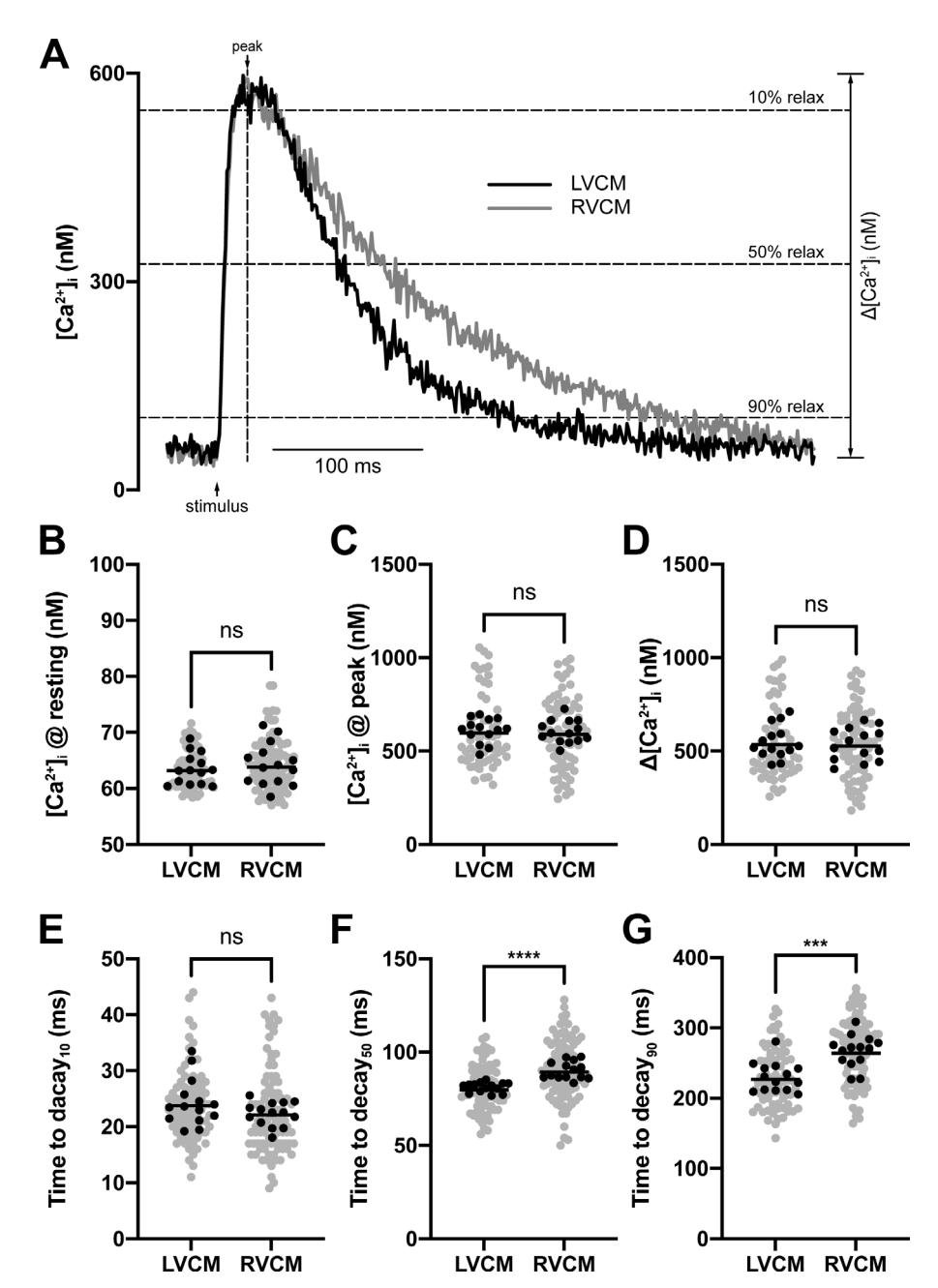


Figure 3. Calcium transients and their parameters in RVCM and LVCM. (A) Representative traces of $\left[\mathsf{Ca}^{2+}\right]_i$ changes evoked by field stimulation in LVCM (black) and RVCM (gray). Summary of the results from LVCM (n = 76, n =14) and RVCM (n = 98, n = 14). (**B-D**) Diastolic [Ca²⁺]_i just before the pulse (B), the peak level (C), and their difference ($\Delta[Ca^{2+}]_i$; D) showed no difference between RVCM and LVCM. (E-G) Time to $decay_{10}$, $decay_{50}$, and $decay_{90}$, representing the time from peak to 10, 50, and 90% decay of Ca2+ transient, respectively. Note the longer times to decay₅₀ and decay₉₀ in RVCM than LVCM. All statistical tests performed using nested t test. ***, P < 0.001; ****, P < 0.0001. The gray dot means the measured value of individual cells, and the block dot represents the average of the measured value for each animal. The black line in the column means average of measured value.

Jeon et al.Lower troponins in rat right ventricle



mathematical integration of the inward current per membrane capacitance ($\int I_{Ca,L}dt \cdot C_m^{-1}$)—was smaller when applying the RVCM-type AP (Fig. 2 H).

Analyses of Ca2+ transient

The Ca²⁺ transient of intact cardiomyocytes triggered by repetitive electrical field stimulation (2 Hz) was observed in cells loaded with fura-2-AM (Fig. 3 A, representative traces). Summarized results from LVCM and RVCM are shown as bar graphs (Fig. 3, B–G). The [Ca²⁺]_i during the diastolic period did not differ between the RVCM and LVCM (Fig. 3 B). Considering the shorter APD and the smaller Ca²⁺ influx via VOCC_L (Figs. 1 and 2), it was anticipated that Δ [Ca²⁺]_i would be smaller in RVCM. However, the peak [Ca²⁺]_i and Δ [Ca²⁺]_i were not different from those of LVCM, indicating a mismatch between AP and Ca²⁺ transient (Fig. 3, C and D). Furthermore, despite the shorter APD, the decay of the Ca²⁺ transient was slower in the RVCM than in the LVCM (Fig. 3, E–G). 14 animals were used for measuring Ca²⁺ transient, and the four parameters analyzed in each animal are depicted in Fig. S6.

In rat ventricular cardiomyocytes, SERCA is mainly responsible for the decay of the Ca²⁺ transient (Bassani et al., 1994). Therefore, we analyzed SERCA activity in RVCM using wholecell patch clamp combined with fura-2 ratiometry. Under the current-clamp configuration, AP-triggering current injections (~1.0 nA, 1 Hz) were applied to confirm that the steady-state Ca²⁺ transient reflected the responses of the Ca²⁺-loaded state of the SR (Fig. 4 A, stimulation). Three Ca²⁺ removal mechanisms, SERCA, NCX, and PMCA, eliminated intracellular Ca2+ into SR and extracellular space in this condition, and the time constant τ_{tran} reflected the sum of the rates of Ca²⁺ removal by the three mechanisms (Fig. 4 B, stimulation). After stopping stimulation, we immediately applied 20 mM of caffeine to induce Ca2+ transient (Fig. 4 A, caffeine). In this condition, where SERCA activity was nullified, NCX and PMCA were involved in the decay of caffeine-induced calcium transient, which could be fitted to a single exponential function (τ_{caff} ; Fig. 4 B, caffeine). As the SR was depleted by the previous caffeine application, the cardiomyocytes were then restimulated by current injection until steady state was achieved (Fig. 4 A, second stimulation). The cardiomyocytes were then superfused with 0 Na/0 Ca solution to inhibit the NCX, and the second application of caffeine induced the Ca^{2+} transient with a slow decay speed (τ_{ONaOCa}) Fig. 4 A). As the SERCA and NCX were inhibited by caffeine and 0 Na/0 Ca bath solution, the decay kinetics of Ca2+ transient would be mainly affected by PMCA (Fig. 4 B, right panel). The decay of the Ca²⁺ transient of this experiment could be fitted to single exponential function (Fig. 4 B).

The time constant reflecting all the three Ca^{2+} removal mechanisms (τ_{tran}) was significantly larger in the RVCM (Fig. 4 C), while the time constant was almost identical when SERCA was neglected (τ_{caff} , Fig. 4 D), implying that the slower Ca^{2+} decay of RVCM was due to the lower SERCA activity. From the three rate constants (k_{tran} , k_{caff} , and k_{ONaOCa}) obtained by taking the reciprocal of time constants (τ_{tran} , τ_{caff} , and τ_{ONaOCa}), the relative contributions made to Ca^{2+} removal by SERCA, NCX, and PMCA (relative rate constant) were determined using the

protocol described by Díaz et al. (2004), with correction for the plausible error from the difference in endogenous buffer (see In situ analysis of the Ca²⁺ binding ratio...). The total rate of Ca²⁺ removal was higher in LVCM than RVCM, mostly because of the 2.23-times-higher relative rate of SERCA in LVCM (Fig. 4 F). The relative NCX and PMCA activity were also lower in RVCM (Fig. 4 F). However, since >89% of the total calcium removal mechanism was performed by SERCA [$(k_{tran} - k_{caff})/k_{tran}$], the difference of NCX and PMCA between two ventricles seems to have a partial effect on the total Ca²⁺ removal rate.

Molecular mechanism of the difference in SERCA activity

To investigate the underlying mechanisms of the observed difference in SERCA activity, we compared the protein amount of SERCA2a, which actively sequesters Ca²⁺ back into the SR lumen to remove intracellular Ca²⁺ (Sathish et al., 2006). When assessed by quantification of bands, the protein level of SERCA2a was not significantly different in the two ventricles (Fig. 5). Because the small difference that was not statistically significant could not account for the difference in SERCA activity, we focused on the endogenous inhibitor of SERCA, PLB, and its phosphorylated form (p-PLB), which relieves the inhibitory function of PLB (Tada and Katz, 1982; Simmerman et al., 1986). We compared the expression of PLB, which was normalized to the expression of internal loading control. The amount of PLB was not different in the two ventricles, while that of p-PLB was lower in RVCM. The ratio of p-PLB to PLB was 0.40 ± 0.039 versus 0.28 ± 0.065, also significantly lower in RVCM (Fig. 5 E).

Ca2+-binding proteins of myofilament components

Although the lower SERCA activity could explain the slower Ca²⁺ decay of RVCM, the similar Ca²⁺ peaks despite the shorter APD suggested additional differences in the Ca²⁺-buffering components of RVCM. We hypothesized that the Ca²⁺-binding myofilament proteins, such as TnC, might be different between RVCM and LVCM. TnC is the major Ca²⁺-binding protein in the cytosol of cardiomyocytes (Smith and Eisner, 2019). The immunoblot assay of the myofilament fraction revealed that the expression levels of TnC, TnI, and TnT were commonly lower in RVCM compared with LVCM (Fig. 5). In contrast, the levels of tropomyosin, desmin, actinin, and myosin binding protein C did not differ between RVCM and LVCM.

Overloading of samples is a widespread problem, termed membrane saturation, that may compromise the reliability of quantitative analysis, especially in enriched samples (Ghosh et al., 2014; Pillai-Kastoori et al., 2020). To overcome this limitation, we performed immunoblot experiments while loading various amounts of protein (1–5 μ g) to find the range of protein amount that does not cause membrane saturation (Fig. S7). In the case of TnI, TnC, and tropomyosin, the signal of protein bands was not saturated up to 5 μ g of protein, while that of TnT showed a saturated signal from 4 μ g of protein (Fig. S7 B). The expression of cTn was lower in RVCM at the unsaturated ranges of protein amount. All the signals of blotting in this experiment were normalized to the total signal of protein using Ponceau S staining as an internal loading control (Gilda and Gomes, 2013; Sander et al., 2019).



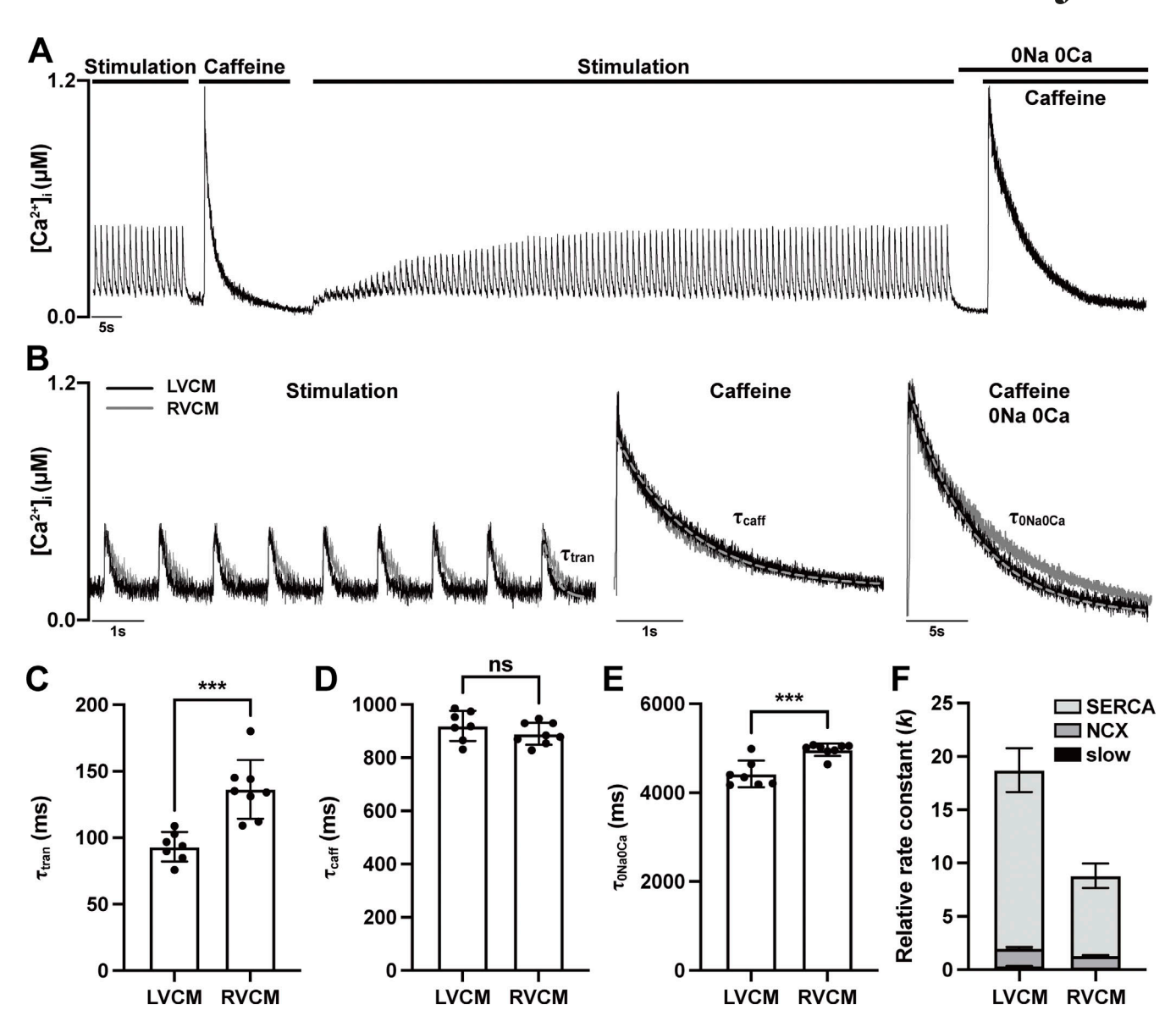


Figure 4. **Analyses of the Ca²⁺ transient and its sequestration by SERCA in RVCM and LVCM. (A)** Under the whole-cell voltage-clamp configuration containing fura-2, repetitive AP-triggering current injections (\sim 1.0 nA, 6 ms, 1 Hz) were applied. The stimulus was halted after confirming the steady-state responses, and fast perfusion of caffeine (20 mM) was applied to evoke caffeine-induced Ca²⁺ transient. After the caffeine treatment, the APs were triggered again, which induced the recovery of Ca²⁺ transient. Then, the bath was perfused with 0 Na/0 Ca solution, followed by the fast transient perfusion of caffeine (20 mM, 1 s). **(B)** The time constants (τ_{tran} , τ_{caff} , and τ_{ONaOCa}) were obtained by fitting the decaying phase of Ca²⁺ transients using single exponential function. **(C-E)** Summary of the time constants (τ_{tran} , τ_{caff} , and τ_{ONaOCa}). The τ_{tran} and τ_{ONaOCa} were longer in RVCM, while τ_{caff} was not different in the two ventricles (n = 7, n = 5). **(F)** The relative rate constants reflecting the relative contributions of Ca²⁺-removal mechanisms are summarized. The relative rate of total Ca²⁺ removal and SERCA activity are significantly lower in RVCM (P < 0.0001). All statistical tests performed using Student's t = 1 test. ***, P < 0.001.

Ca^{2+} binding ratio of the endogenous calcium buffer (κ_s) in RVCM

Cytosolic Ca²⁺ buffers in cardiomyocytes are composed of various components, including proteins such as TnC, calmodulin, and myosin. The major Ca²⁺ buffers in the physiological range of Ca²⁺ concentration (100–1,000 nM) are regulatory Ca²⁺-specific binding sites of TnC and active sequestration by SERCA. The other constituents (calmodulin and ATP) are quantitatively small or have dissociation constants that are widely different from the physiological [Ca²⁺]_i (Ca²⁺/Mg²⁺-binding site of TnC and myosin light chain; Smith and Eisner, 2019). We analyzed

the κ_S values of the RVCM and LVCM after excluding the factors from calcium-induced calcium release (CICR), SERCA, and NCX using the SERCA inhibitor (thapsigargin, 2.5 μ M), RYR activator (caffeine, 20 mM), and Na⁺-free bath solution (Fig. 6 and Fig. 7 A; see Eq. 1 in Materials and methods).

When depolarizing pulses (from -40 to 10 mV, 100 ms, 1 Hz) were applied in 0 Na/2 Ca solution, a cumulative increase in $[Ca^{2+}]_i \le 2 \mu M$ was observed during the 8-10 consecutive pulses (upper panel of Fig. 7 B). Because the Ca^{2+} influx via $VOCC_L$ was the sole source of $\Delta[Ca^{2+}]_i$, the integral of calcium currents was obtained (Fig. 7 B, bottom panel). The integrated



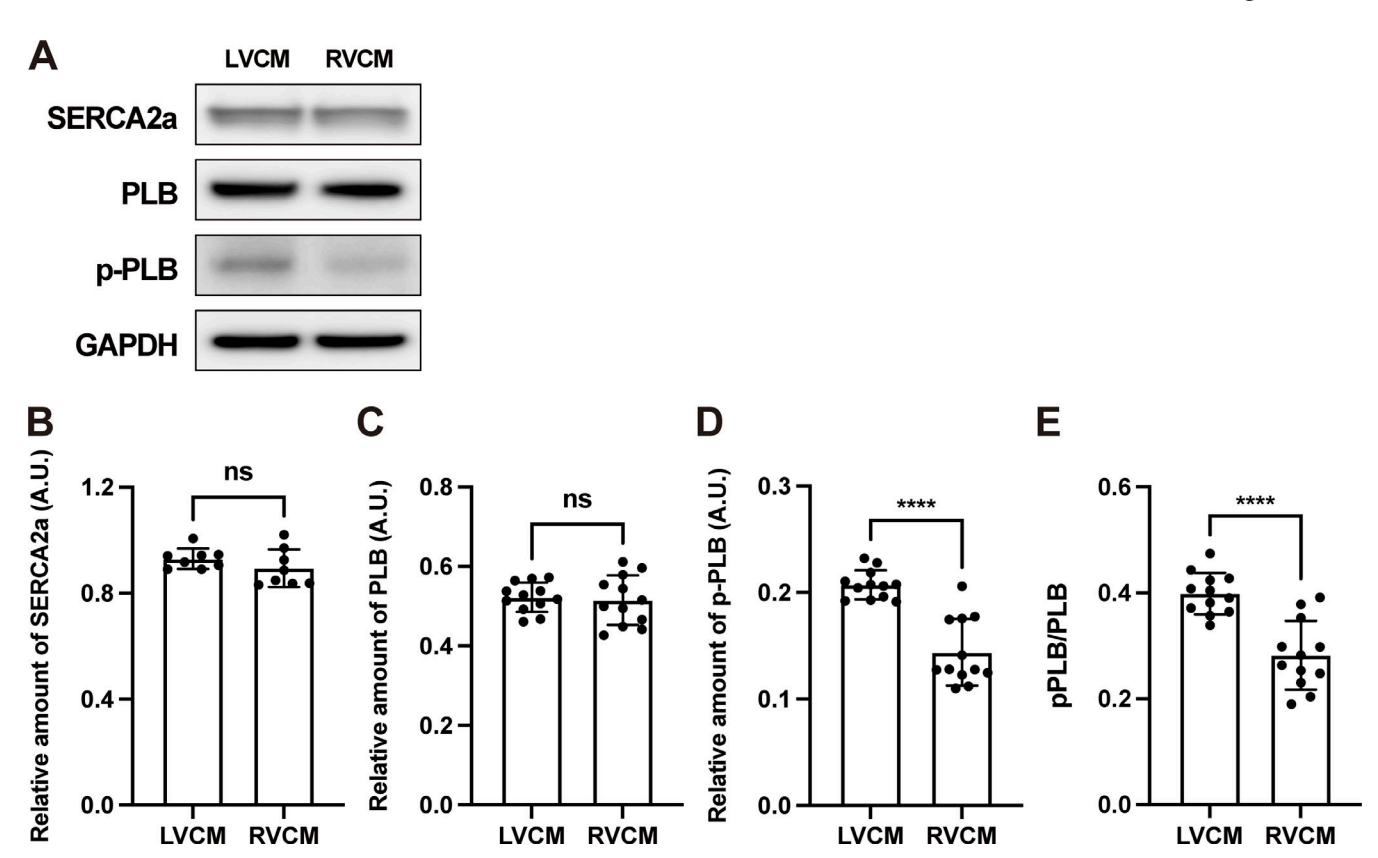


Figure 5. **The protein expression of SERCA and regulatory proteins. (A)** The protein of two ventricles was extracted and blotted using SDS-PAGE. Representative blotting results are depicted. **(B–D)** Protein expression was normalized to GAPDH and summarized (*n* = 12). The amount of SERCA2a and PLB is not different in the two ventricles, while p-PLB is significantly lower in RVCM. **(E)** The ratio of p-PLB to PLB is also significantly lower in RVCM. All statistical tests performed using Student's *t* test. ****, P < 0.0001.

Ca²⁺ influx was divided by the accessible cell volume (vol_{ac} , in Materials and methods) to obtain the calculated net increase in $[Ca^{2+}]$ ($\Delta[Ca^{2+}]_{tot,cal}$). The median values of $[Ca^{2+}]_i$ before and immediately after the individual pulses were measured. The relationship between κ_B and the median $[Ca^{2+}]$ was plotted (circles in Fig. 8, A and B), and the κ_B and $[B]_{tot}$ values were obtained by fitting Eq. 2 (see Materials and methods).

In the above experimental measurement, it should be noted that when using fura-2, an "added-buffer" condition (Neher, 1995), the contribution from fura-2 ($Fura_{tot}$) has to be excluded from $[B]_{tot}$ to deduce the endogenous calcium buffer, $[S]_{tot}$ (Fig. 8, C-E). Because we know the dissociation constant of fura-2 ($K_{d.fura-2}$) from the in vitro calibration mimicking the cytosolic environment (see Materials and methods; Fig. S1) and the effective total concentration of fura-2 from Eq. 3 ([fura-2]_{tot}; Fig. 8 D), the correlation between the Ca²⁺-binding ratio of fura-2 (κ_{fura-2}) and the corresponding median [Ca²⁺] could be fitted to a differential form of the Michaelis-Menten equation (square symbols in Fig. 8, A and B). Finally, the differences between κ_B and κ_{fura-2} , i.e., κ_S could be obtained by subtraction, the result of which was fitted by Eq. 1 to calculate the two parameters of the endogenous buffer: the total concentration of the intrinsic buffer $([S]_{tot})$ and the dissociation constant of the intrinsic buffer $(K_{d.S})$. In accordance with the expression level of myofilament proteins, $[S]_{tot}$ of RVCM was actually smaller than that of LVCM

(195.8 ± 19.61 μ M versus 127.5 ± 21.09 μ M; Fig. 8 E). The reported dissociation constant of TnC ($K_{d,TnC}$ < 0.6 μ M, from Smith and Eisner, 2019) is smaller than that of measured intrinsic buffer, which was 0.90 ± 0.156 μ M in LVCM. Therefore, the calcium affinity of the endogenous buffer would be lower in RVCM owing to the lower proportion of troponin among the total intrinsic buffer. Consistently, the $K_{d,S}$ values were larger in RVCM than in LVCM ($K_{d,S}$ of RVCM = 1.21 ± 0.239 μ M). Using the parameters obtained from the experiments (κ_B , κ_S , κ_{fura-2} , [B]_{tot}, [fura-2]_{tot}, [S]_{tot}), we calculated the bound Ca²⁺ (calculated bound Ca²⁺) from the median [Ca²⁺] using the Michaelis–Menten equation. The calculated buffering power of RVCM was lower than that of LVCM (Fig. 8, G and H).

SL changes and the kinetics of contraction relaxation

The above differences in the factors determining the Ca^{2+} transient kinetics (e.g., lower SERCA activity and endogenous Ca^{2+} buffer) suggested differential features of contraction-relaxation between RVCM and LVCM. In the IonOptix experiment, we analyzed the SL changes induced by repetitive electrical field stimulation (2 Hz; Fig. 8 A). 20 animals were used for measuring SL, and 6 parameters analyzed for each animal are depicted in Fig. S8. The basal SL of RVCM during the diastolic phase appeared to be longer than that of LVCM, but not statistically significantly when nested t test was



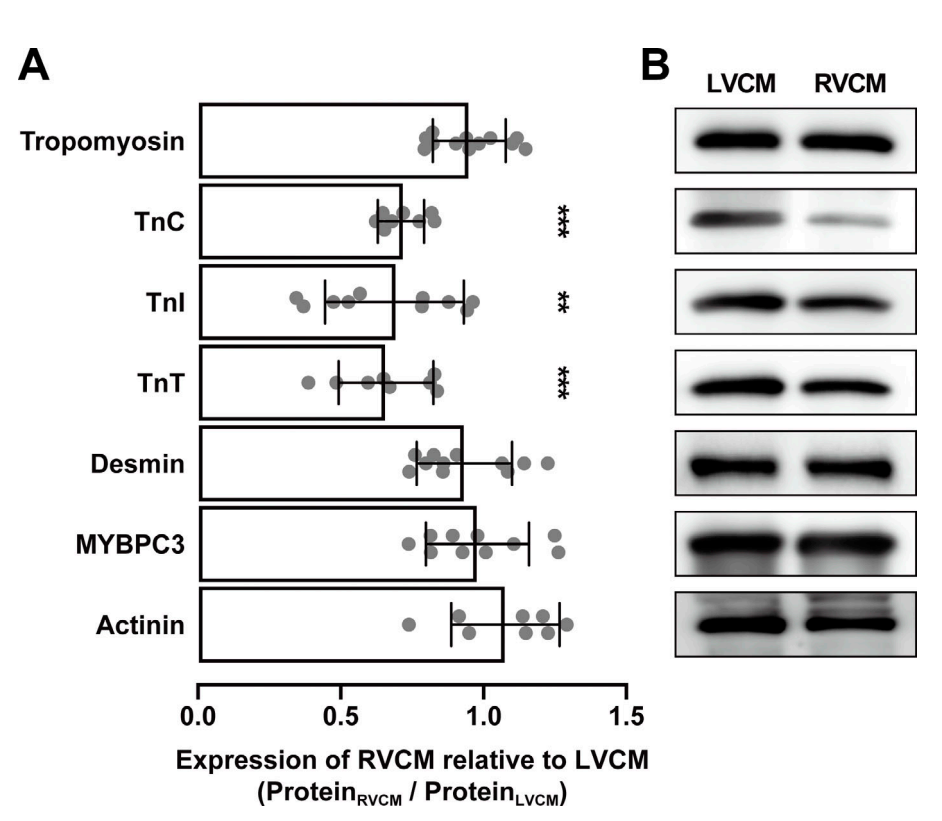


Figure 6. Lower expression of troponins in RVCM. (A) The myofilament fraction of cardiomyocytes was extracted and blotted using SDS-PAGE. TnC, TnI, and TnT are commonly lower in RVCM than in LVCM, while the expression level of tropomyosin, desmin, actinin, and myosin binding protein C (MYBPC) are not different between RVCM and LVCM. Expression levels of protein were normalized to that of LVCM and plotted as ratios (n = 8-12). (B) Representative blotting results are depicted. All statistical test performed using Student's t test.

applied (Fig. 9 C, P = 0.190). The average maximum shortening in 10 consecutive pulses (Δ SL) was smaller in RVCM (Fig. 9 D). The percent normalized values (Δ SL/SL %) were also smaller in RVCM than in LVCM (Fig. 9 E). To clarify the difference in relaxation speed, the relative SL changes normalized to the peak SL were analyzed (Fig. 9 B). The relaxation speed was lower in RVCM (Fig. 9, F-H), which seems to be consistent with the slower decay of the Ca²⁺ transient in RVCM (Fig. 3, E-G).

The physiological heart rate of rat is faster (5–6 Hz) than the pacing rate in the present study (2 Hz). To confirm whether the different pacing rates might have induced the different contractile properties between RVCM and LVCM, the SL analysis was conducted at different pacing frequencies (2–6 Hz), where the smaller Δ SL and the slower relaxation speed in RVCM were consistently observed (Fig. S9).

Mathematical simulation of the Ca²⁺ transient and contraction

Finally, we recapitulated the experimental findings from the Ca^{2+} transient and the single-cell contraction (half-SL change, ΔSL_{half}) by using a combinational computational model of rat ventricular cardiomyocytes constructed from two mathematical models (Pandit et al., 2001; Negroni and Lascano, 2008). Because the models were based on the experimental values obtained from LVCM, the three parameters were modified: the larger I_{to} , the lower SERCA activity, and the lower cTn expression (Fig. 10; for the AP simulation, see Fig. 2). To consider the kinetics of Ca^{2+} binding with TnC, we also calculated the differential parameter expressing the flux of Ca^{2+} to the cTn (dJ_{TRPN}/dt) according to the I_{tropn} in Negroni and Lascano (2008) (Fig. 10 B).

When a higher I_{to} ($g_{to} \cdot 1.31$) was introduced, all three amplitudes (Ca^{2+} transient, dJ_{TRPN}/dt , and ΔSL_{half}) were decreased (Fig. 10 A, upper panels), which was consistent with the effect of the RVCM AP-clamp on $I_{Ca,L}$ (Fig. 2 H). The combined lowering of SERCA activity ($I_{SERCA} \cdot 0.44$) with the higher I_{to} slowed the decay of the Ca^{2+} transient and ΔSL_{half} , resulting in their amplitudes being only slightly increased (Fig. 10, middle panels, blue traces). In contrast, the combined lowering of cTn (cTn · 0.65) with a higher I_{to} significantly increased the amplitude of the Ca^{2+} transient while decreasing dJ_{TRPN}/dt and ΔSL_{half} (Fig. 10, middle panels, green lines). By combining the changes in the three parameters, I_{to} , SERCA, and cTn, the simulated Ca^{2+} transient and ΔSL_{half} were close to the experimental data of the RVCM when compared with the simulated LVCM (Fig. 10, lower panels).

Discussion

In addition to the previously known differences in electrophysiology (larger I_{to}) and lower SERCA activity in RVCM (Afzal and Dhalla, 1992; Molina et al., 2016), our present study demonstrated novel aspects of biventricular differences regarding E–C coupling, the lower expression of cTn that seems to underlie the lower Ca²⁺ buffering capacity and smaller contraction in RVCM. The lower SERCA activity and cTn in RVCM could explain the apparent mismatches between the AP versus Ca²⁺ transient as well as the Ca²⁺ transient versus Δ SL, which was reproduced by mathematical simulations.

Mismatch between AP and Ca2+ transient

The whole-cell patch clamp showed shorter APD and larger I_{to} in RVCM than in LVCM (Fig. 1 and Fig. 2, A–C). These findings are



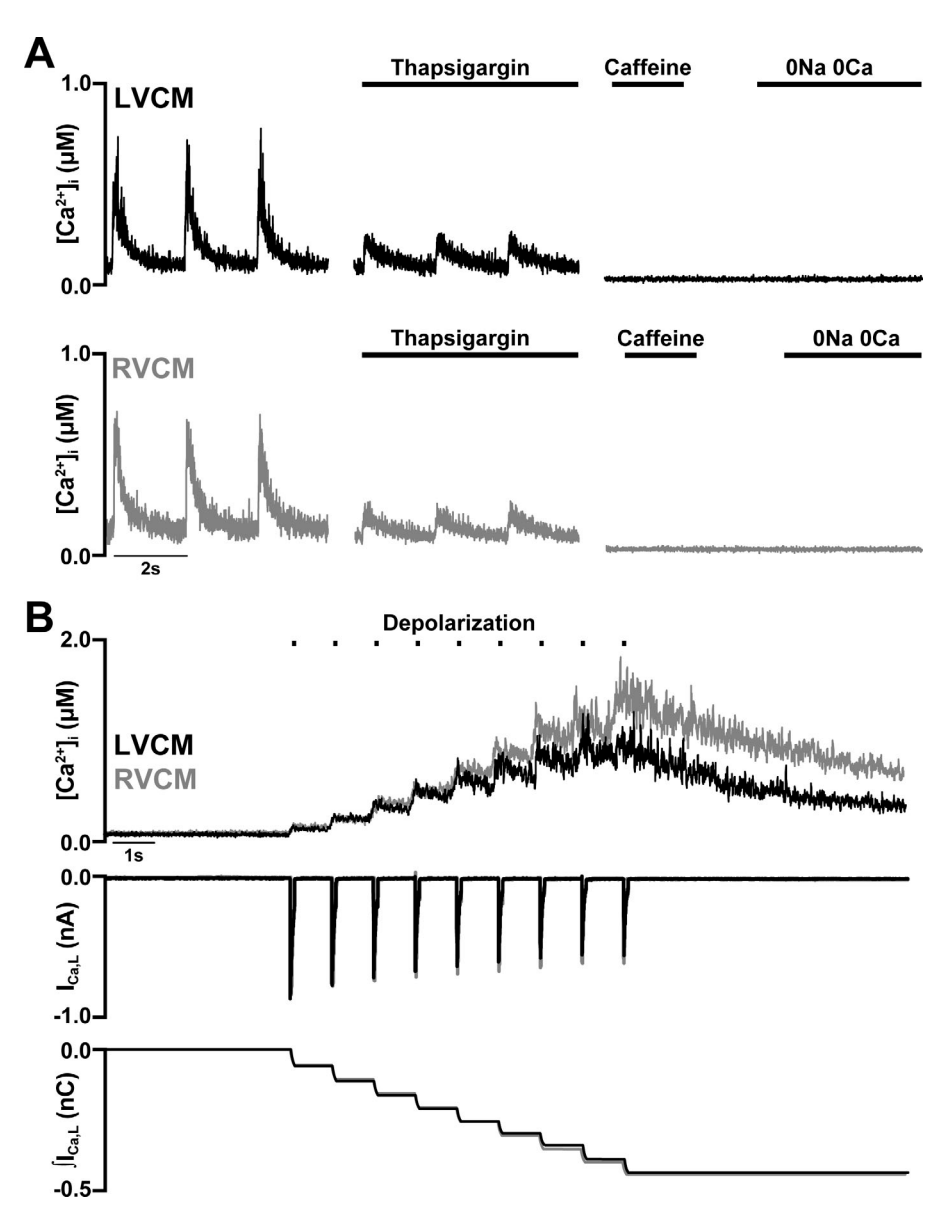


Figure 7. Measurement of the Ca2+ binding ratio of cardiomyocytes. (A) Representative traces of [Ca²⁺]_i observed in the preparatory protocols before the measurement of the Ca2+ buffering ratio in the whole-cell voltage clamp of the fura-2 pentapotassium salt loaded cardiomyocytes. After confirming the Ca2+ transient evoked by step pulses (from -70 to 0 mV, 200 ms, 0.5 Hz), SERCA was inhibited by thapsigargin while continuing the stimulation pulses. Then, 20 mM caffeine was applied to confirm the depleted state of the SR. Finally, the bath was changed from NT to 0 Na/0 Ca solution to inhibit NCX. (B) After reaching the steady-state condition, a higher rate of depolarizing pulses (from -40 mV to 0 mV, 100 ms, 1 Hz, 9-10 times) was applied to induce inward Ca²⁺ current (middle panel) and associated increase of [Ca²⁺]_i (upper panel). The inward Ca2+ current was integrated and plotted as the quantity of electric charge (lower panel) for the calculation of Ca²⁺ binding ratio (see Materials and methods).

consistent with those of previous studies on rodent cardiomyocytes (Di Diego et al., 1996; Brunet et al., 2004). Because the $I_{Ca,L}$ was not different (Fig. 2, D-F), the higher I_{to} seems to be responsible for the faster repolarization in RVCM, which was also reproduced by the mathematical electrophysiological model of rat cardiomyocytes (Fig. 2 G). Heterogeneity of electrical properties has also been observed in LVCM of the epi- and endocardium (Watanabe et al., 1983; Kondo et al., 2006). In fact, a study comparing RVCM with epi- and endocardial LVCM showed that the AP configuration of RVCM was similar to that of epi-LVCM (Kondo et al., 2006). Regrettably, we did not rigorously divide the LVCM from the epi- and endocardium. Nevertheless, the consistent statistical significance of the different parameters in AP and Ito suggested that the LVCM were a relatively homogeneous group close to the endocardial myocytes (Figs. 1 and 2).

Despite the shorter APD and smaller net Ca^{2+} influx via $VOCC_L$, the amplitude of the Ca^{2+} transient was not different between RVCM and LVCM (Fig. 3). Because the amount of Ca^{2+}

released from the SR (CICR) is mainly responsible for the final amplitude of Ca^{2+} transient in cardiomyocytes (Eisner et al., 2017), one has to also consider the efficiency of CICR when comparing the biventricular difference. Unfortunately, we could not directly evaluate the CICR efficiency or activity of RYR channels. Because the inactivation of $VOCC_L$ is largely affected by the $[Ca^{2+}]$ of the junctional space near RYR, an indirect estimation from the inactivation speed of $I_{Ca,L}$ in the perforated whole-cell patch clamp could be provided. The identical time constants of inactivation kinetics did not support the hypothesis that CICR efficiency was higher in RVCM. Therefore, the SR Ca^{2+} -release via CICR could be smaller in the beating RVCM than in LVCM because of the smaller Ca^{2+} influx during the shorter AP.

Taking these findings together, the more plausible explanation for the mismatch between the APD and the Ca²⁺ transient was the lower level of endogenous Ca²⁺ buffer and removal mechanism. In cardiomyocytes, it is known that only 1% of the total calcium increase could be experimentally detected as free



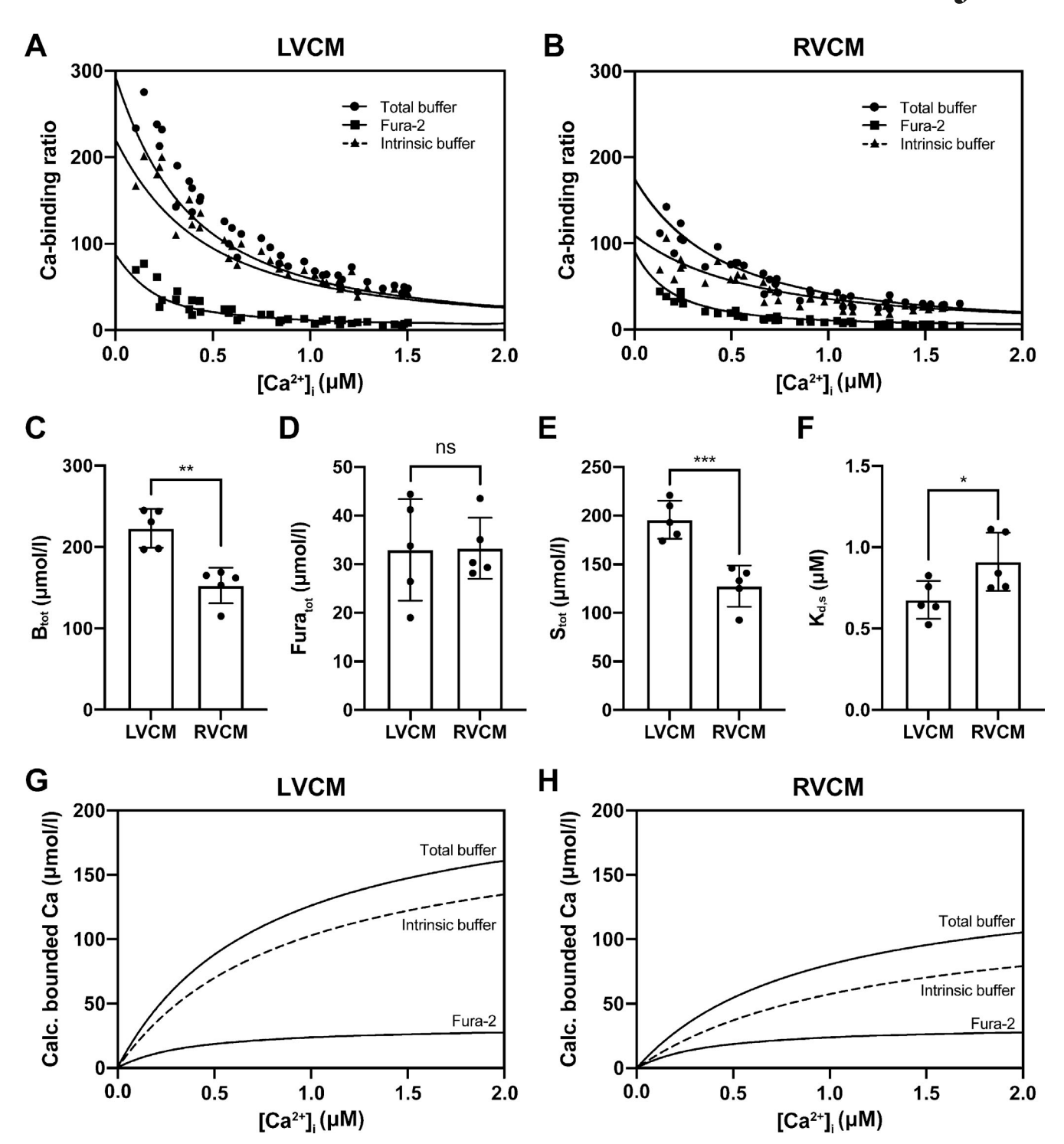


Figure 8. Calculation of total cytosolic Ca²⁺ buffers in RVCM and LVCM. (A and B) Ca²⁺ binding ratio values from five times of experiments for LVCM (A) and RVCM (B) were plotted as a function of $[Ca^{2+}]_i$. Total buffer was the sum of fura-2 and hypothetical Ca^{2+} binding species S. The variables reflecting chemical properties of buffers were calculated by fitting curves using Eq. 2 (total buffer) and Eq. 1 (intrinsic buffer). (C and D) The amount of total buffer (B_{tot}) is larger in LVCM (C), while that of fura-2 (F_{total}) is not different (D). (E) S_{tot} total amount of intrinsic buffer, is also larger in LVCM. (F) The dissociation constants of intrinsic buffer ($K_{d,S}$) were acquired using Eq. 3. (G and H) Ca^{2+} bound to total buffer, fura-2, and intrinsic buffer was calculated (Calc.) as a function of $[Ca^{2+}]_i$ with the differential equation and buffer parameters. The dotted lines indicate the Ca^{2+} bound to the intrinsic buffer. All statistical tests performed using Student's t test (n = 5). *, P < 0.05; ***, P < 0.01; ***, P < 0.001.



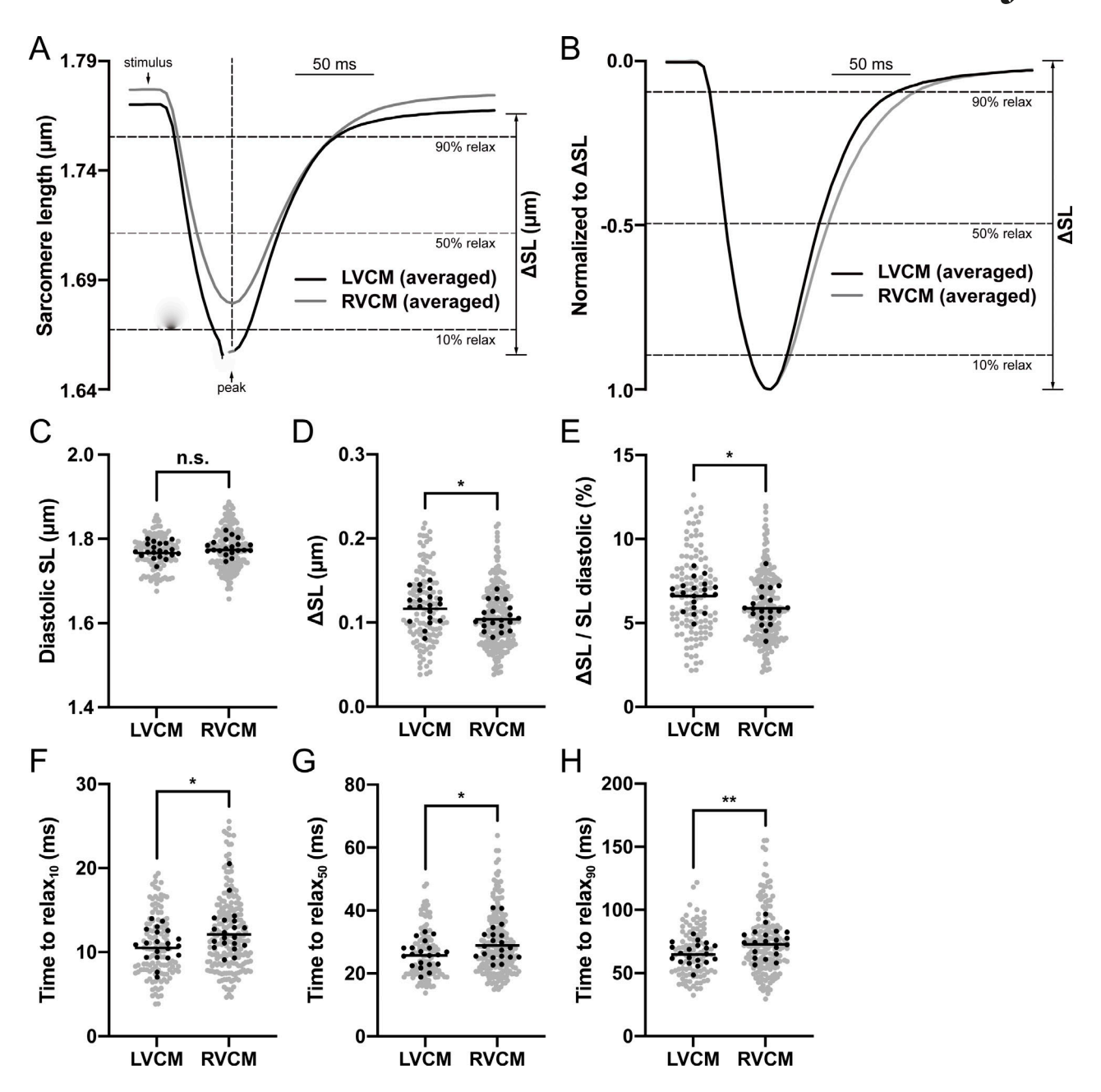


Figure 9. **SL** and its changes (Δ SL) in RVCM and LVCM. (A and B) Averaged traces of SL (A) and normalized Δ SL (B) in LVCM (n = 102, n = 20, black line) and RVCM (n = 170, n = 20, gray lines). (**C-F**) Summaries comparing the diastolic SL (C), Δ SL (D), and the percent ratio of Δ SL/diastolic SL in each cell (E). (**F-H**) Time to relax₅₀, relax₅₀, and relax₉₀ representing the time from peak to 10, 50, and 90% relaxation of Δ SL, respectively. Note the longer relaxation times in RVCM than LVCM. All statistical tests performed using nested t test. The gray dot means the measured value of individual cells, and the block dot represents the average of the measured value for each animal. The black line in the column means average of measured value.

Ca²⁺; 99% is bound to the cytosolic buffers or removed by SERCA, NCX, and PMCA (Fabiato, 1983; Hove-Madsen and Bers, 1993). Among the latter Ca²⁺ removal mechanisms, SERCA predominantly operates in rodent cardiomyocytes (Bassani et al, 1994; Díaz et al, 2004). A previous study using rat myocardium demonstrated slower SERCA in the SR vesicles isolated from RVCM than in those isolated from LVCM (Sathish et al., 2006). A similar finding was also confirmed in the present study using intact cardiomyocytes (Fig. 4), and the underlying mechanism of difference in SERCA activity was due to the difference in the phosphorylation states of PLB, which was lower in RVCM

(Fig. 5). However, the lower SERCA activity appears to be more responsible for the slower rate of the Ca²⁺ transient decay than the instantaneous increase, which could also be simulated by mathematical modeling (Fig. 10).

Among the cytoplasmic proteins of cardiomyocytes, TnC could provide quantitatively effective Ca^{2+} buffering capacity in the physiological range of $\Delta[Ca^{2+}]_i$ (Pan and Solaro, 1987; Smith and Eisner, 2019). The Ca^{2+} -binding site of TnC is classified into two categories: Ca^{2+} -specific site and Ca^{2+}/Mg^{2+} -binding site (Robertson et al., 1981). Because the Ca^{2+}/Mg^{2+} -binding site with low K_d values (0.0195 μ M, from Pan and Solaro, 1987) would be



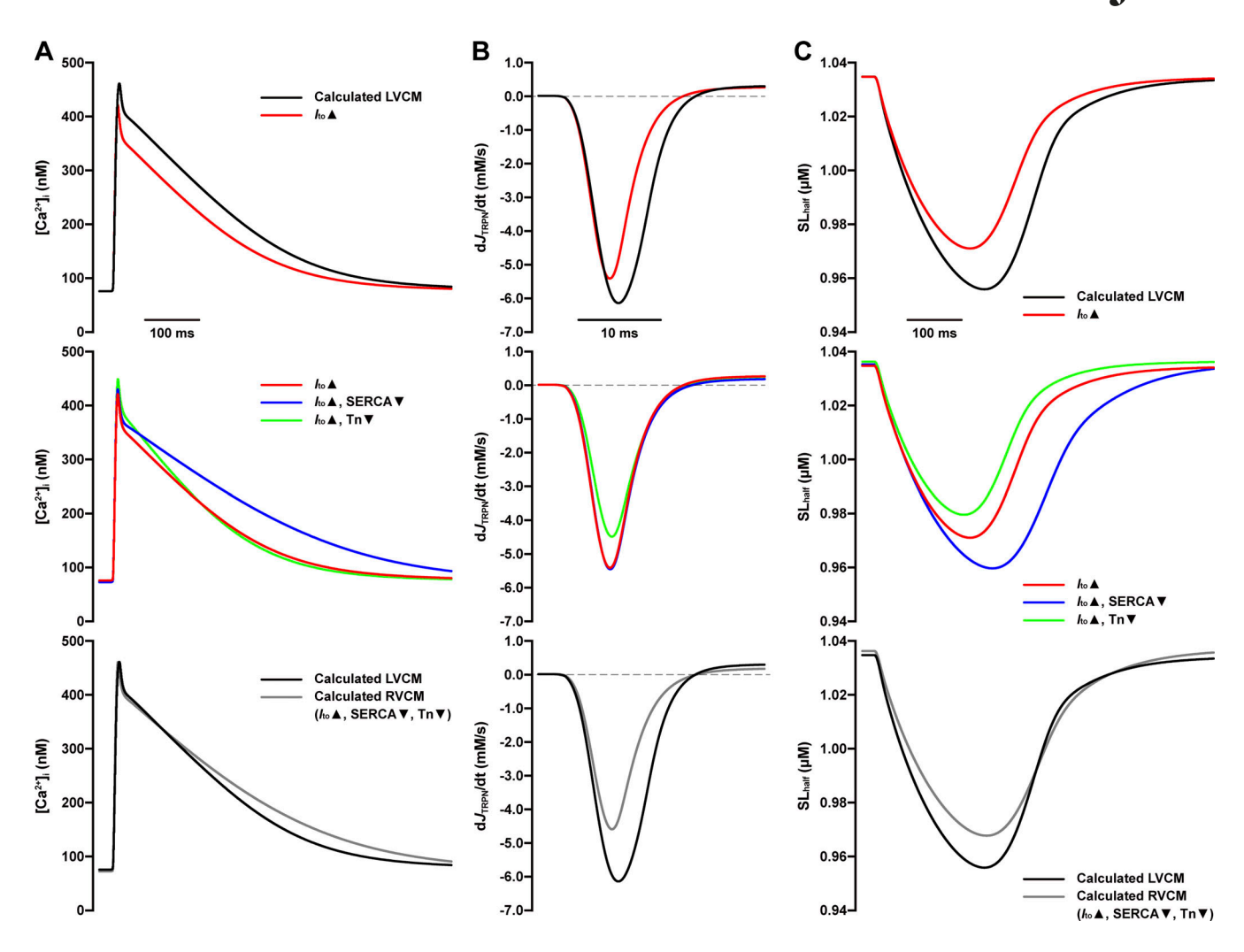


Figure 10. Simulated contribution of the differences in I_{to} , SERCA, and cTn levels to the kinetics of Ca²⁺ transient and of ΔSL in RVCM. (A and B) Calculated Ca²⁺ transients (A), Ca²⁺ flux to the troponin fraction (B), and half sarcomere shortening (ΔSL_{half}) obtained from the computations based on the models by Pandit et al. (2001) and Negroni and Lascano (2008). The black lines correspond to the computational changes in the control LVCM (calculated LVCM). The results by increasing the conductance of I_{to} by 31% alone ($g_{to} \cdot 1.31$, red line) and combined with decreased SERCA (40.0% of control, blue line) or with lowered cTn (67% of control, green line). The combined changes of all three parameters are displayed by the gray line. (C) Effect of applying all the three parameter changes ($g_{to} \cdot 1.31$, $I_{SERCA} \cdot 0.44$, and cTn · 0.64) on the Ca²⁺ transient (gray line). *, P < 0.05; **, P < 0.01.

largely occupied by Ca^{2+} or Mg^{2+} at their resting levels, binding with the Ca^{2+} -specific site in TnC would change dynamically during the cardiac cycle. In this study, the expression of TnC, along with TnI and TnT, was actually lower by $\sim 30\%$ in RVCM than LVCM (Figs. 6 and S7). Based on the buffering properties of cTn, we propose that the differential Ca^{2+} buffering capacity could explain the mismatch between APD and the amplitude of the Ca^{2+} transient.

The apparently lower ratio of cTn over other myofilament proteins was an unexpected finding. According to the recent cryo-electron microcopy study of the cardiac myofilament structure, cTn attaches to a specific position of tropomyosin at every seventh actin monomer. Therefore, the ratio of actin, tropomyosin, and cTn would be a tight stoichiometry of 7:1:1 (Oda et al., 2020; Yamada et al., 2020). In this respect, the lower cTn in RVCM could imply a discordance between the amount of tropomyosin and cTn and putative instability of the myofilament complexes. Unfortunately, our data from

immunoblotting experiments could not provide a reasonable explanation for the controversy. Nevertheless, a previous 2-D electrophoresis analysis of porcine heart also suggested the relatively lower level of TnC than tropomyosin in the RV than LV (Phillips et al., 2011). In addition, a differential in-gel electrophoresis combined with mass spectrometry study of human cardiac tissues suggested higher tropomyosin in comparison with TnI in LV than RV (Su et al., 2015). The studies including our present study suggested a difference in cTn/tropomyosin between RV and LV. Although it is not very likely, the regularity of association between cTn and tropomyosin in RVCM might not be as strict as in LVCM. Otherwise, the immunoblot results might include putative soluble components of the myofilament proteins that are different between RV and LV.

To precisely compare the intrinsic Ca²⁺-buffering capacity, we calibrated the in situ Ca²⁺ buffering properties using the added-buffer method (Berlin et al., 1994; Neher, 1995). For this



purpose, it was necessary to define the buffer components as a collective Ca2+-binding species (S), described by a single dissociation constant $(K_{d,S})$ and concentration ([S]_{tot}). Although S partially reflects components other than TnC such as calmodulin, ATP, and myosin, it mostly depends on the Ca²⁺-binding affinity and concentration of TnC under physiological conditions (Smith and Eisner, 2019). The calibration and analysis actually revealed that the Ca²⁺-binding ratio, $K_{d,S}$, and $[S]_{tot}$ were lower in RVCM than in LVCM (Figs. 7 and 8). Taken together, these data suggest that the similar amplitudes of Ca2+ transients despite their shorter APD were due to the lower expression of the Ca2+-binding TnC in RVCM. However, there might be another plausible difference in posttranslational modification of TnC affecting Ca²⁺-binding properties (Robertson et al., 1982; Blanchard and Solaro, 1984), which remains to be investigated in the future.

Interventricular difference in SERCA activity

In rodent cardiomyocytes, SERCA is a major functional Ca²⁺ buffer along with cTn (Berlin et al., 1994; Smith and Eisner, 2019). The calculation of Ca²⁺ buffering using the methods by Berlin et al. (1994) could not take SERCA activity into account. To overcome the limitation, we calculated this effect of lower SERCA activity using mathematical in silico models (Fig. 10). Although the lower cTn increased the height of the Ca2+ transient to a greater extent, the lower SERCA activity also had an effect on the $\Delta[Ca^{2+}]_i$. It appeared that those two features of RVCM, the lower expression of cTn and the activity of SERCA, were acting in concert in $\Delta[Ca^{2+}]_i$ of RVCM. Notably, the reduction in sarcomere shortening due to lower cTn expression became less significant by the combined lowering of SERCA (Fig. 10 C, green line versus gray line). Considering the unavoidable lag time for the Ca2+-dependent operation of myofilament proteins, the combined contribution of SERCA as well as cTn would determine the final amplitude of contraction, that is, ΔSL.

Although Kondo et al. (2006) reported no difference in SERCA2a gene expression and its inhibitory regulator PLB, Sathish et al. (2006) showed lower levels of the protein SERCA2a and PLB proteins in RVCM than LVCM. Functional studies have suggested lower SERCA activity in RVCM (Afzal and Dhalla, 1992; Sathish et al., 2006), consistent with the present study. However, there was a quantitative difference; the previous functional studies showed four to five times slower maximum velocity of SR Ca²⁺ uptake (V_{max}) in RVCM (Afzal and Dhalla, 1992; Sathish et al., 2006). Our analysis of SERCA from the analysis of rate constants showed a 2.23-fold larger rate constant in RVCM than LVCM (Fig. 4). Even though the measured variables were not the same (V_{max}) versus τ), the difference was still significant. A plausible explanation is the discrepancy in measuring processes: SRenriched homogenate (Sathish et al., 2006) versus in situ Ca²⁺ imaging (present study). Regardless of the quantitative difference, a lower SERCA activity and lower phosphorylation of PLB might be the key features of E-C coupling in RVCM.

Contractility of RVCM

Here, we found another notable point in the E-C coupling process: shorter ΔSL despite the similar $\Delta [Ca^{2+}]_i$ in RVCM, which might be explained by the lower expression of cTn. Under the physiological environment, the RV is exposed to smaller afterload with more rapid pressure decline in cardiac cycle, and the P-V loop shows shorter isovolumic contraction time with slower decay of systolic pressure (Dell'Italia and Walsh, 1988). The macroscopic properties of RV such as the thinner wall and nonoblique geometry of myofibers are thought to be associated with the hemodynamic differences (Redington et al., 1988; Sengupta et al., 2006; Walker and Buttrick, 2013). Although it is difficult to extrapolate the properties of a single myocyte to the whole ventricle, the smaller ΔSL and slower relaxation of RVCM might partly explain the triangular shape of the P-V loop of RV.

Although not directly comparable with our present results, a previous study using a point mutation in TnI (K118C) with dominant-negative effects showed decreased contractility and shorter length of cardiomyocytes in transgenic mice (Wei and Jin, 2014). Another case was missense mutations in the Ca²⁺-specific binding site of TnC (E59D and D75Y), which was discovered from a patient diagnosed with idiopathic dilated cardiomyopathy. Rat cardiomyocytes with adenoviral expression of D75Y showed less cell shortening than wild-type cardiomyocytes, even without changes in the Ca²⁺ transient (Lim et al., 2008). In addition, the increased proteolytic activity and subsequent lowering of cTn were responsible for the impaired contractility and relaxation in ventricular hypertrophy (van der Laarse, 2002). These studies suggest that the expression, Ca²⁺binding affinity, and Ca²⁺ sensitivity of cTn closely regulate cell shortening. Although we did not directly investigate the Ca2+dependent contraction of permeabilized cardiomyocytes to analyze Ca2+ sensitivity, we cautiously interpret that the smaller ΔSL might be due to, at least partly, the lower amount of cTn in RVCM. To confirm this hypothesis, it is worth investigating the relationship between the role of lowered cTn and smaller ΔSL of RVCM.

In the computational simulations combining the previous mathematical models and the kinetics of Ca^{2+} binding to the cTn (Pandit et al., 2001; Negroni and Lascano, 2008), we calculated the Ca^{2+} flux to the myofilament fraction (J_{TRPN}) and its time-dependent change (dJ_{TRPN}/dt ; Fig. 10 B). This approach was based on the assumption that the Ca^{2+} flux to the myofilament is totally engaged in the Tn- Ca^{2+} state cycle. In the Negroni and Lascano (2008) model, the force and length of contraction depend on the number of cross-bridges, that is, the amount of effective troponin. In this context, the cTn-dependent Δ SL in the virtual simulation would be a self-evident result. Nevertheless, the intriguing point of our present study is that the expression of cTn was actually lower in RVCM (Figs. 6 and S7).

Although the heart rate of rats is faster than that of humans, 5–6 Hz (300–350 bpm), we used a 2-Hz frequency for pacing cardiomyocytes due to constraints in the experimental system using isolated single cells. For instance, myocytes showed tendency of deterioration at high rates of stimulating frequencies, especially when loaded with fura-2, limiting the simultaneous rerecording of Ca^{2+} transient and ΔSL . In the IonOptix system



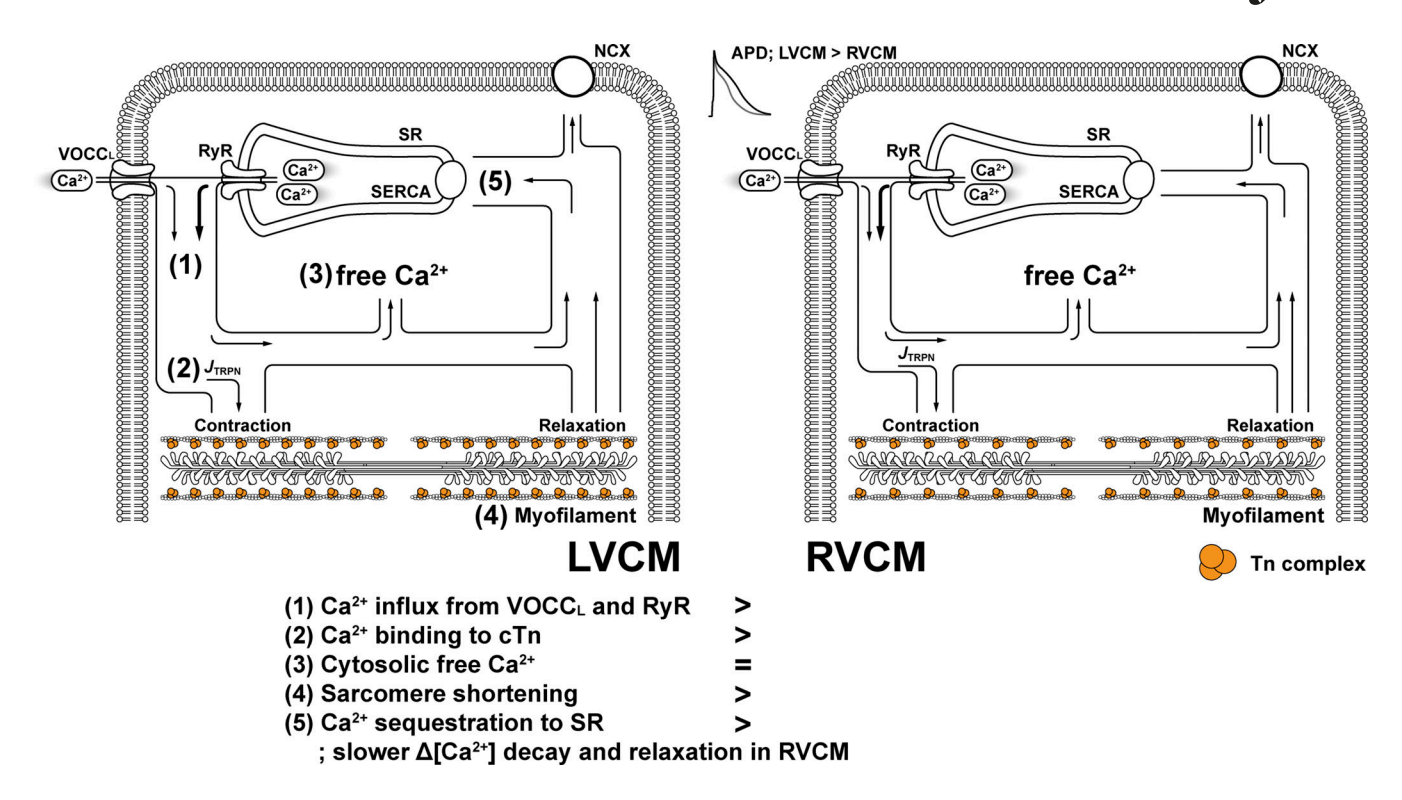


Figure 11. **Comparison of LVCM and RVCM.** Diagrams presented here are consistent with our hypothesis where RVCM has less cTn (orange-filled circles in myofilament) and lower SERCA activity. The width of pipe represents the amount of Ca^{2+} flux between the subcellular domains, approximately. (1) RVCM showed smaller Ca^{2+} influx from VOCC_L and RYR due to short AP. Note that the pipe from VOCC_L and RYR of RVCM is thinner than that of LVCM. (2) The amount of Ca^{2+} flux to myofilament (J_{TRPN}) is smaller in RVCM due to the lower expression of the cTn complex. (3) Reflecting this difference, the free Ca^{2+} measured by Ca^{2+} indicator looks the same in height despite lower Ca^{2+} influx via VOCC_L and efflux via RYR. (4) The sarcomere shortening is also smaller in RVCM, with lower expression of cTn, the contraction apparatus. (5) The thinner duct implies the lower activity of SERCA, which is reflected in the slower Ca^{2+} decay and sarcomere relaxation in RVCM.

solely recording SL, we could confirm that the differences in contractility (Δ SL and relaxation speed) between RVCM and LVCM were maintained at higher pacing frequencies (Fig. S9).

It was notable that both RVCM and LVCM showed a tendency toward decreasing ΔSL at the higher pacing rates (Fig. S9, B and C), suggesting a kind of negative force–frequency relation (FFR). In large animals, the ventricular myocytes exhibit positive FFR due to increased SR Ca²⁺ content (Kurihara and Sakai, 1985; Joulin et al., 2009). In contrast, rat cardiomyocytes exhibit very weakly positive or even negative FFR (Banijamali et al., 1991; Maier et al., 1998; Janssen and Periasamy, 2007) owing to their higher SR Ca²⁺ content, even at the low stimulation frequencies (Shattock and Bers, 1989; Maier et al., 2000).

While both RVCM and LVCM showed frequency-dependent acceleration of relaxation (FDAR), slower relaxation of RVCM was consistently observed at the physiological pacing frequency (Fig. S9, E and F). In physiological conditions, FDAR might be essential to refill more rapidly between beats (Schouten, 1990; Hussain et al., 1997). It was reported that the FDAR was SR dependent and modulated by SERCA (Bassani et al., 1995). Although calcium transient was not directly compared at the higher pacing frequencies, accelerated Ca²⁺ removal could be inferred from the recordings of Δ SL. Also, we cautiously concluded that slower recovery of Ca²⁺ transient of RVCM would be conserved at the physiological heart rate of rodents.

Pathophysiological implications

Along with the anatomic biventricular differences such as the ventricular wall thickness and the muscle fiber band folding pattern, the lower cardiac troponin and the smaller ΔSL in the RVCM might be related to the pathophysiological responses of the RV in vivo. Changes in Ca^{2+} sensitivity make a significant contribution to the contractility of cardiomyocytes during disease progression (Belin et al., 2007; Marston and de Tombe, 2008). Because the phosphorylation of TnI plays a critical role in the modulation of Ca^{2+} sensitivity, the lower cTn might be partly responsible for the less effective adaptation to the increased afterload.

The importance of Ca²⁺ buffering has been suggested in genetically engineered rats to express parvalbumin, a Ca²⁺-binding protein, in cardiomyocytes (Wahr et al., 1999). Although there was little effect on the peak Ca²⁺ transient due to the slow Ca²⁺ binding kinetics of parvalbumin, the gene-transferred cardiomyocytes showed accelerated decay of [Ca²⁺]_i, implying improved diastolic performance of cardiomyocytes. These effects of parvalbumin suggest the potential importance of slow buffers, including the Ca²⁺/Mg²⁺-binding site on TnC, in the development and consequences of heart failure, as recently mentioned by Smith and Eisner (2019). While we did not directly measure the slow-acting buffer power of cardiomyocytes, the lower expression of cTn in RVCM might be partly associated with the vulnerability of the RV.



Beat-to-beat alternation of cardiac AP (alternans) is regarded as an arrhythmia mechanism with an increased risk of sudden cardiac death (Kulkarni et al., 2019). The delayed Ca²⁺ decay or abnormal Ca²⁺ signal could underlie the alternans, as suggested by the reduced probability of alternans by injecting EGTA into cardiomyocytes (Baudenbacher et al., 2008). The increased Ca²⁺ buffer could suppress the pathological Ca²⁺ waves triggered by SR Ca²⁺ release (Nivala et al., 2012; Bovo et al., 2015). In addition to the buffering effects on Ca²⁺ sparks, there was an idea that incomplete recovery at the time of the next stimulus followed by the slow decay of the Ca²⁺ transient might be attributed to the induction of alternans (Baudenbacher et al., 2008). In fact, genetically up-regulated SERCA2a suppressed the genesis of alternans (Lyon et al., 2011; Cutler et al., 2012). Interestingly, ventricular arrhythmia was more frequent in RV myocardial infarction than in inferior or anterior wall LV myocardial infarction (Mehta et al., 2001; Ondrus et al., 2013). According to the present study, we cautiously suppose that the lower Ca²⁺ buffer by TnC and the slower Ca²⁺ sequestration by SERCA in RVCM implied higher susceptibility to ventricular arrhythmia in the above conditions.

In summary, from the comparative analysis of the E–C coupling between the RVCM and LVCM of rat, in addition to the electrical difference (higher I_{to} and shorter AP), we found lower Ca²⁺-buffering mechanisms in RVCM, that is, TnC and SERCA (Fig. 11). The lower expression of TnC could explain the dual mismatch phenomena in the biventricular differences of the E–C coupling. The pathophysiological implications of the present findings, such as the putative changes in TnC expression, require further investigation in right heart disease models.

Acknowledgments

David A. Eisner served as editor.

This work was supported by the National Research Foundation of Korea funded by the Ministry of Science and ICT, Republic of Korea to S.J. Kim (grants NRF-2018R1D1A1B07048998, NRF-2018R1A5A2025964, and NRF-2021R1A2C2007243), and by EDISON (Education-Research Integration through Simulation on the Net; NRF-2016M3C1A6936605). This work was also supported by a grant of the M.D., Ph.D./Medical Scientist Training Program through the Korea Health Industry Development Institute to Y.K. Jeon, funded by the Ministry of Health and Welfare, Republic of Korea.

The authors declare no competing financial interests.

Author contributions: conception and design: Y.K. Jeon, J. Jang, J.B. Youm, Y.H. Zhang, and S.J. Kim; collection of data: Y.K. Jeon, J.W. Kwon, J. Jang, S.W. Choi, J. Woo, S.H. Cho, and B.I. Yu; analysis and/or interpretation: Y.K. Jeon, J.W. Kwon, J. Jang, Y.S. Chun, J.B. Youm, Y.H. Zhang, and S.J. Kim; manuscript writing: Y.K. Jeon, J.B. Youm, Y.H. Zhang, and S.J. Kim. All the authors reviewed and approved the final version of the manuscript.

Submitted: 26 April 2021 Accepted: 6 January 2022

References

- Afzal, N., and N.S. Dhalla. 1992. Differential changes in left and right ventricular SR calcium transport in congestive heart failure. Am. J. Physiol. 262:H868-H874. https://doi.org/10.1152/ajpheart.1992.262.3.H868
- Banijamali, H.S., W.D. Gao, B.R. MacIntosh, and H.E. ter Keurs. 1991. Force-interval relations of twitches and cold contractures in rat cardiac trabeculae. Effect of ryanodine. Circ. Res. 69:937–948. https://doi.org/10.1161/01.RES.69.4.937
- Bassani, J.W., R.A. Bassani, and D.M. Bers. 1994. Relaxation in rabbit and rat cardiac cells: species-dependent differences in cellular mechanisms. J. Physiol. 476:279-293. https://doi.org/10.1113/jphysiol.1994.sp020130
- Bassani, R.A., A. Mattiazzi, and D.M. Bers. 1995. CaMKII is responsible for activity-dependent acceleration of relaxation in rat ventricular myocytes. Am. J. Physiol. 268:H703-H712. https://doi.org/10.1152/ajpheart .1995.268.2.H703
- Baudenbacher, F., T. Schober, J.R. Pinto, V.Y. Sidorov, F. Hilliard, R.J. Solaro, J.D. Potter, and B.C. Knollmann. 2008. Myofilament Ca2+ sensitization causes susceptibility to cardiac arrhythmia in mice. J. Clin. Invest. 118: 3893–3903. https://doi.org/10.1172/JCI36642
- Belin, R.J., M.P. Sumandea, E.J. Allen, K. Schoenfelt, H. Wang, R.J. Solaro, and P.P. de Tombe. 2007. Augmented protein kinase C-alpha-induced myofilament protein phosphorylation contributes to myofilament dysfunction in experimental congestive heart failure. Circ. Res. 101: 195–204. https://doi.org/10.1161/CIRCRESAHA.107.148288
- Berlin, J.R., J.W. Bassani, and D.M. Bers. 1994. Intrinsic cytosolic calcium buffering properties of single rat cardiac myocytes. Biophys. J. 67: 1775-1787. https://doi.org/10.1016/S0006-3495(94)80652-6
- Blanchard, E.M., and R.J. Solaro. 1984. Inhibition of the activation and troponin calcium binding of dog cardiac myofibrils by acidic pH. Circ. Res. 55:382-391. https://doi.org/10.1161/01.RES.55.3.382
- Borzak, S., R.A. Kelly, B.K. Krämer, Y. Matoba, J.D. Marsh, and M. Reers. 1990. In situ calibration of fura-2 and BCECF fluorescence in adult rat ventricular myocytes. Am. J. Physiol. 259:H973-H981. https://doi.org/10 .1152/ajpheart.1990.259.3.H973
- Bovo, E., S.R. Mazurek, M. Fill, and A.V. Zima. 2015. Cytosolic Ca²⁺ buffering determines the intra-SR Ca²⁺ concentration at which cardiac Ca²⁺ sparks terminate. *Cell Calcium*. 58:246–253. https://doi.org/10.1016/j
- Brunet, S., F. Aimond, H. Li, W. Guo, J. Eldstrom, D. Fedida, K.A. Yamada, and J.M. Nerbonne. 2004. Heterogeneous expression of repolarizing, voltage-gated K+ currents in adult mouse ventricles. J. Physiol. 559: 103–120. https://doi.org/10.1113/jphysiol.2004.063347
- Carneiro-Júnior, M.A., T.N. Prímola-Gomes, J.F. Quintão-Júnior, L.R. Drummond, V.N. Lavorato, F.R. Drummond, L.B. Felix, E.M. Oliveira, J.S. Cruz, A.J. Natali, and J.G. Mill. 2013. Regional effects of low-intensity endurance training on structural and mechanical properties of rat ventricular myocytes. J Appl Physiol (1985). 115:107–115. https://doi.org/10.1152/japplphysiol.00041.2013
- Cheung, J.Y., D.L. Tillotson, R.V. Yelamarty, and R.C. Scaduto Jr. 1989. Cytosolic free calcium concentration in individual cardiac myocytes in primary culture. Am. J. Physiol. 256:C1120-C1130. https://doi.org/10.1152/ajpcell.1989.256.6.C1120
- Cooper, P.J., C. Soeller, and M.B. Cannell. 2010. Excitation-contraction coupling in human heart failure examined by action potential clamp in rat cardiac myocytes. J. Mol. Cell. Cardiol. 49:911-917. https://doi.org/10.1016/j.yjmcc.2010.04.012
- Cutler, M.J., X. Wan, B.N. Plummer, H. Liu, I. Deschenes, K.R. Laurita, R.J. Hajjar, and D.S. Rosenbaum. 2012. Targeted sarcoplasmic reticulum Ca2+ ATPase 2a gene delivery to restore electrical stability in the failing heart. Circulation. 126:2095–2104. https://doi.org/10.1161/CIRCULATIONAHA.111.071480
- Dell'Italia, L.J., and R.A. Walsh. 1988. Acute determinants of the hangout interval in the pulmonary circulation. Am. Heart J. 116:1289–1297. https://doi.org/10.1016/0002-8703(88)90454-1
- Di Diego, J.M., Z.Q. Sun, and C. Antzelevitch. 1996. I(to) and action potential notch are smaller in left vs. right canine ventricular epicardium. Am. J. Physiol. 271:H548–H561. https://doi.org/10.1152/ajpheart.1996.271.2 .H548
- Díaz, M.E., H.K. Graham, and A.W. Trafford. 2004. Enhanced sarcolemmal Ca2+ efflux reduces sarcoplasmic reticulum Ca2+ content and systolic Ca2+ in cardiac hypertrophy. Cardiovasc. Res. 62:538-547. https://doi.org/10.1016/j.cardiores.2004.01.038
- Duggal, D., S. Requena, J. Nagwekar, S. Raut, R. Rich, H. Das, V. Patel, I. Gryczynski, R. Fudala, Z. Gryczynski, et al. 2017. No Difference in Myosin Kinetics and Spatial Distribution of the Lever Arm in the Left



- and Right Ventricles of Human Hearts. Front. Physiol. 8:732. https://doi.org/10.3389/fphys.2017.00732
- Eisner, D.A. 2021. Pseudoreplication in physiology: More means less. J. Gen. Physiol. 153:e202012826. https://doi.org/10.1085/jgp.202012826
- Eisner, D.A., J.L. Caldwell, K. Kistamás, and A.W. Trafford. 2017. Calcium and Excitation-Contraction Coupling in the Heart. *Circ. Res.* 121:181–195. https://doi.org/10.1161/CIRCRESAHA.117.310230
- Fabiato, A. 1983. Calcium-induced release of calcium from the cardiac sarcoplasmic reticulum. Am. J. Physiol. 245:C1–C14. https://doi.org/10.1152/ aipcell.1983.245.1.C1
- Fabiato, A., and F. Fabiato. 1979. Calculator programs for computing the composition of the solutions containing multiple metals and ligands used for experiments in skinned muscle cells. J. Physiol. (Paris). 75: 463-505
- Foschi, M., M. Di Mauro, F. Tancredi, C. Capparuccia, R. Petroni, L. Leonzio, S. Romano, S. Gallina, M. Penco, M. Cibelli, and A. Calafiore. 2017. The Dark Side of the Moon: The Right Ventricle. *J. Cardiovasc. Dev. Dis.* 4:18. https://doi.org/10.3390/jcdd4040018
- Friedberg, M.K., and A.N. Redington. 2014. Right versus left ventricular failure: differences, similarities, and interactions. Circulation. 129: 1033-1044. https://doi.org/10.1161/CIRCULATIONAHA.113.001375
- Ghosh, R., J.E. Gilda, and A.V. Gomes. 2014. The necessity of and strategies for improving confidence in the accuracy of western blots. Expert Rev. Proteomics. 11:549–560. https://doi.org/10.1586/14789450.2014.939635
- Gilda, J.E., and A.V. Gomes. 2013. Stain-Free total protein staining is a superior loading control to β -actin for Western blots. *Anal. Biochem.* 440: 186–188. https://doi.org/10.1016/j.ab.2013.05.027
- Harris, D.M., G.D. Mills, X. Chen, H. Kubo, R.M. Berretta, V.S. Votaw, L.F. Santana, and S.R. Houser. 2005. Alterations in early action potential repolarization causes localized failure of sarcoplasmic reticulum Ca2+ release. Circ. Res. 96:543–550. https://doi.org/10.1161/01.RES.0000158966.58380.37
- Hove-Madsen, L., and D.M. Bers. 1993. Passive Ca buffering and SR Ca uptake in permeabilized rabbit ventricular myocytes. *Am. J. Physiol.* 264: C677–C686. https://doi.org/10.1152/ajpcell.1993.264.3.C677
- Hussain, M., G.A. Drago, J. Colyer, and C.H. Orchard. 1997. Rate-dependent abbreviation of Ca2+ transient in rat heart is independent of phospholamban phosphorylation. Am. J. Physiol. 273:H695–H706. https://doi .org/10.1152/ajpheart.1997.273.2.H695
- Jang, J.H., M.J. Kang, G.P. Ko, S.J. Kim, E.C. Yi, and Y.H. Zhang. 2015. Identification of a novel splice variant of neuronal nitric oxide synthase, nNOSβ, in myofilament fraction of murine cardiomyocytes. Nitric Oxide. 50:20–27. https://doi.org/10.1016/j.niox.2015.07.005
- Janssen, P.M., and M. Periasamy. 2007. Determinants of frequency-dependent contraction and relaxation of mammalian myocardium. J. Mol. Cell. Cardiol. 43:523-531. https://doi.org/10.1016/j.yjmcc.2007.08.012
- Jin, C.Z., J.H. Jang, Y. Wang, J.G. Kim, Y.M. Bae, J. Shi, C.R. Che, S.J. Kim, and Y.H. Zhang. 2012. Neuronal nitric oxide synthase is up-regulated by angiotensin II and attenuates NADPH oxidase activity and facilitates relaxation in murine left ventricular myocytes. J. Mol. Cell. Cardiol. 52: 1274–1281. https://doi.org/10.1016/j.vjmcc.2012.03.013
- Joulin, O., S. Marechaux, S. Hassoun, D. Montaigne, S. Lancel, and R. Neviere. 2009. Cardiac force-frequency relationship and frequency-dependent acceleration of relaxation are impaired in LPS-treated rats. Crit. Care. 13: R14. https://doi.org/10.1186/cc7712
- Katsube, Y., H. Yokoshiki, L. Nguyen, M. Yamamoto, and N. Sperelakis. 1998. L-type Ca2+ currents in ventricular myocytes from neonatal and adult rats. Can. J. Physiol. Pharmacol. 76:873–881. https://doi.org/10.1139/y98-076
- Knollmann, B.C., A.N. Katchman, and M.R. Franz. 2001. Monophasic action potential recordings from intact mouse heart: validation, regional heterogeneity, and relation to refractoriness. J. Cardiovasc. Electrophysiol. 12:1286–1294. https://doi.org/10.1046/j.1540-8167.2001.01286.x
- Kondo, R.P., D.A. Dederko, C. Teutsch, J. Chrast, D. Catalucci, K.R. Chien, and W.R. Giles. 2006. Comparison of contraction and calcium handling between right and left ventricular myocytes from adult mouse heart: a role for repolarization waveform. J. Physiol. 571:131–146. https://doi.org/ 10.1113/jphysiol.2005.101428
- Konishi, M., A. Olson, S. Hollingworth, and S.M. Baylor. 1988. Myoplasmic binding of fura-2 investigated by steady-state fluorescence and absorbance measurements. *Biophys. J.* 54:1089–1104. https://doi.org/10.1016/ S0006-3495(88)83045-5
- Kulkarni, K., F.M. Merchant, M.B. Kassab, F. Sana, K. Moazzami, O. Sayadi, J.P. Singh, E.K. Heist, and A.A. Armoundas. 2019. Cardiac

- Alternans: Mechanisms and Clinical Utility in Arrhythmia Prevention. J. Am. Heart Assoc. 8:e013750. https://doi.org/10.1161/JAHA.119.013750
- Kurihara, S., and T. Sakai. 1985. Effects of rapid cooling on mechanical and electrical responses in ventricular muscle of guinea-pig. J. Physiol. 361: 361-378. https://doi.org/10.1113/jphysiol.1985.sp015650
- Lim, C.C., H. Yang, M. Yang, C.K. Wang, J. Shi, E.A. Berg, D.R. Pimentel, J.K. Gwathmey, R.J. Hajjar, M. Helmes, et al. 2008. A novel mutant cardiac troponin C disrupts molecular motions critical for calcium binding affinity and cardiomyocyte contractility. *Biophys. J.* 94:3577–3589. https://doi.org/10.1529/biophysi.107.112896
- Lyon, A.R., M.L. Bannister, T. Collins, E. Pearce, A.H. Sepehripour, S.S. Dubb, E. Garcia, P. O'Gara, L. Liang, E. Kohlbrenner, et al. 2011. SERCA2a gene transfer decreases sarcoplasmic reticulum calcium leak and reduces ventricular arrhythmias in a model of chronic heart failure. Circ. Arrhythm. Electrophysiol. 4:362–372. https://doi.org/10.1161/CIRCEP.110.961615
- Maier, L.S., R. Brandes, B. Pieske, and D.M. Bers. 1998. Effects of left ventricular hypertrophy on force and Ca2+ handling in isolated rat myocardium. Am. J. Physiol. 274:H1361-H1370. https://doi.org/10.1152/ajpheart.1998.274.4.H1361
- Maier, L.S., D.M. Bers, and B. Pieske. 2000. Differences in Ca(2+)-handling and sarcoplasmic reticulum Ca(2+)-content in isolated rat and rabbit myocardium. J. Mol. Cell. Cardiol. 32:2249–2258. https://doi.org/10 .1006/jmcc.2000.1252
- Marston, S.B., and P.P. de Tombe. 2008. Troponin phosphorylation and myofilament Ca2+-sensitivity in heart failure: increased or decreased? J. Mol. Cell. Cardiol. 45:603-607. https://doi.org/10.1016/j.yjmcc.2008.07 004
- Mathias, R.T., I.S. Cohen, and C. Oliva. 1990. Limitations of the whole cell patch clamp technique in the control of intracellular concentrations. *Biophys. J.* 58:759-770. https://doi.org/10.1016/S0006-3495(90)82418-8
- Mehta, S.R., J.W. Eikelboom, M.K. Natarajan, R. Diaz, C. Yi, R.J. Gibbons, and S. Yusuf. 2001. Impact of right ventricular involvement on mortality and morbidity in patients with inferior myocardial infarction. J. Am. Coll. Cardiol. 37:37–43. https://doi.org/10.1016/S0735-1097(00)01089-5
- Molina, C.E., D.M. Johnson, H. Mehel, R.L. Spätjens, D. Mika, V. Algalarrondo, Z.H. Slimane, P. Lechêne, N. Abi-Gerges, H.J. van der Linde, et al. 2014. Interventricular differences in β-adrenergic responses in the canine heart: role of phosphodiesterases. *J. Am. Heart Assoc.* 3:e000858. https://doi.org/10.1161/JAHA.114.000858
- Molina, C.E., J. Heijman, and D. Dobrev. 2016. Differences in Left Versus Right Ventricular Electrophysiological Properties in Cardiac Dysfunction and Arrhythmogenesis. Arrhythm. Electrophysiol. Rev. 5:14-19. https://doi.org/10.15420/aer.2016.8.2
- Negroni, J.A., and E.C. Lascano. 2008. Simulation of steady state and transient cardiac muscle response experiments with a Huxley-based contraction model. J. Mol. Cell. Cardiol. 45:300–312. https://doi.org/10.1016/j.yjmcc.2008.04.012
- Neher, E. 1995. The use of fura-2 for estimating Ca buffers and Ca fluxes.

 Neuropharmacology. 34:1423–1442. https://doi.org/10.1016/0028-3908(95)
 00144-U
- Nivala, M., C.Y. Ko, M. Nivala, J.N. Weiss, and Z. Qu. 2012. Criticality in intracellular calcium signaling in cardiac myocytes. *Biophys. J.* 102: 2433–2442. https://doi.org/10.1016/j.bpj.2012.05.001
- Oda, T., H. Yanagisawa, and T. Wakabayashi. 2020. Cryo-EM structures of cardiac thin filaments reveal the 3D architecture of troponin. *J. Struct. Biol.* 209:107450. https://doi.org/10.1016/j.jsb.2020.107450
- Ondrus, T., J. Kanovsky, T. Novotny, I. Andrsova, J. Spinar, and P. Kala. 2013. Right ventricular myocardial infarction: From pathophysiology to prognosis. Exp. Clin. Cardiol. 18:27–30.
- Pan, B.S., and R.J. Solaro. 1987. Calcium-binding properties of troponin C in detergent-skinned heart muscle fibers. J. Biol. Chem. 262:7839–7849. https://doi.org/10.1016/S0021-9258(18)47644-2
- Pandit, S.V., R.B. Clark, W.R. Giles, and S.S. Demir. 2001. A mathematical model of action potential heterogeneity in adult rat left ventricular myocytes. *Biophys. J.* 81:3029–3051. https://doi.org/10.1016/S0006 -3495(01)75943-7
- Phillips, D., A.M. Aponte, R. Covian, E. Neufeld, Z.X. Yu, and R.S. Balaban. 2011. Homogenous protein programming in the mammalian left and right ventricle free walls. *Physiol. Genomics.* 43:1198–1206. https://doi.org/10.1152/physiolgenomics.00121.2011
- Pillai-Kastoori, L., A.R. Schutz-Geschwender, and J.A. Harford. 2020. A systematic approach to quantitative Western blot analysis. Anal. Biochem. 593:113608. https://doi.org/10.1016/j.ab.2020.113608



- Redington, A.N., H.H. Gray, M.E. Hodson, M.L. Rigby, and P.J. Oldershaw. 1988. Characterisation of the normal right ventricular pressure-volume relation by biplane angiography and simultaneous micromanometer pressure measurements. Br. Heart J. 59:23–30. https://doi.org/10.1136/ hrt.59.1.23
- Robertson, S.P., J.D. Johnson, and J.D. Potter. 1981. The time-course of Ca2+exchange with calmodulin, troponin, parvalbumin, and myosin in response to transient increases in Ca2+. *Biophys. J.* 34:559–569. https://doi.org/10.1016/S0006-3495(81)84868-0
- Robertson, S.P., J.D. Johnson, M.J. Holroyde, E.G. Kranias, J.D. Potter, and R.J. Solaro. 1982. The effect of troponin I phosphorylation on the Ca2+-binding properties of the Ca2+-regulatory site of bovine cardiac troponin. J. Biol. Chem. 257:260–263. https://doi.org/10.1016/S0021-9258(19)68355-9
- Sander, H., S. Wallace, R. Plouse, S. Tiwari, and A.V. Gomes. 2019. Ponceau S waste: Ponceau S staining for total protein normalization. Anal. Biochem. 575:44–53. https://doi.org/10.1016/j.ab.2019.03.010
- Sathish, V., A. Xu, M. Karmazyn, S.M. Sims, and N. Narayanan. 2006. Mechanistic basis of differences in Ca2+ -handling properties of sar-coplasmic reticulum in right and left ventricles of normal rat myocardium. Am. J. Physiol. Heart Circ. Physiol. 291:H88-H96. https://doi.org/10.1152/ajpheart.01372.2005
- Satoh, H., L.M. Delbridge, L.A. Blatter, and D.M. Bers. 1996. Surface:volume relationship in cardiac myocytes studied with confocal microscopy and membrane capacitance measurements: species-dependence and developmental effects. Biophys. J. 70:1494–1504. https://doi.org/10.1016/ S0006-3495(96)79711-4
- Schouten, V.J. 1990. Interval dependence of force and twitch duration in rat heart explained by Ca2+ pump inactivation in sarcoplasmic reticulum. J. Physiol. 431:427-444. https://doi.org/10.1113/jphysiol.1990.sp018338
- Sengupta, P.P., J. Korinek, M. Belohlavek, J. Narula, M.A. Vannan, A. Jahangir, and B.K. Khandheria. 2006. Left ventricular structure and function: basic science for cardiac imaging. J. Am. Coll. Cardiol. 48:1988–2001. https://doi.org/10.1016/j.jacc.2006.08.030
- Shattock, M.J., and D.M. Bers. 1989. Rat vs. rabbit ventricle: Ca flux and intracellular Na assessed by ion-selective microelectrodes. *Am. J. Physiol.* 256:C813–C822. https://doi.org/10.1152/ajpcell.1989.256.4.C813
- Sikkel, M.B., D.P. Francis, J. Howard, F. Gordon, C. Rowlands, N.S. Peters, A.R. Lyon, S.E. Harding, and K.T. MacLeod. 2017. Hierarchical statistical

- techniques are necessary to draw reliable conclusions from analysis of isolated cardiomyocyte studies. *Cardiovasc. Res.* 113:1743–1752. https://doi.org/10.1093/cvr/cvx151
- Simmerman, H.K., J.H. Collins, J.L. Theibert, A.D. Wegener, and L.R. Jones. 1986. Sequence analysis of phospholamban. Identification of phosphorylation sites and two major structural domains. *J. Biol. Chem.* 261: 13333–13341. https://doi.org/10.1016/S0021-9258(18)69309-3
- Smith, G.L., and D.A. Eisner. 2019. Calcium Buffering in the Heart in Health and Disease. Circulation. 139:2358-2371. https://doi.org/10.1161/ CIRCULATIONAHA.118.039329
- Su, Y.R., M. Chiusa, E. Brittain, A.R. Hemnes, T.S. Absi, C.C. Lim, and T.G. Di Salvo. 2015. Right ventricular protein expression profile in end-stage heart failure. *Pulm. Circ.* 5:481–497. https://doi.org/10.1086/682219
- Sweeney, H.L., and D.W. Hammers. 2018. Muscle Contraction. Cold Spring Harb. Perspect. Biol. 10:a023200. https://doi.org/10.1101/cshperspect.a023200
- Tada, M., and A.M. Katz. 1982. Phosphorylation of the sarcoplasmic reticulum and sarcolemma. Annu. Rev. Physiol. 44:401–423. https://doi.org/10 .1146/annurev.ph.44.030182.002153
- van der Laarse, A. 2002. Hypothesis: troponin degradation is one of the factors responsible for deterioration of left ventricular function in heart failure. Cardiovasc. Res. 56:8-14. https://doi.org/10.1016/ S0008-6363(02)00534-5
- Wahr, P.A., D.E. Michele, and J.M. Metzger. 1999. Parvalbumin gene transfer corrects diastolic dysfunction in diseased cardiac myocytes. Proc. Natl. Acad. Sci. USA. 96:11982-11985. https://doi.org/10.1073/pnas.96.21.11982
- Walker, L.A., and P.M. Buttrick. 2013. The right ventricle: biologic insights and response to disease: updated. *Curr. Cardiol. Rev.* 9:73–81.
- Watanabe, T., L.M. Delbridge, J.O. Bustamante, and T.F. McDonald. 1983. Heterogeneity of the action potential in isolated rat ventricular myocytes and tissue. Circ. Res. 52:280-290. https://doi.org/10.1161/01.RES.52.3.280
- Wei, H., and J.P. Jin. 2014. A dominantly negative mutation in cardiac troponin I at the interface with troponin T causes early remodeling in ventricular cardiomyocytes. Am. J. Physiol. Cell Physiol. 307:C338–C348. https://doi.org/10.1152/ajpcell.00053.2014
- Yamada, Y., K. Namba, and T. Fujii. 2020. Cardiac muscle thin filament structures reveal calcium regulatory mechanism. Nat. Commun. 11:153. https://doi.org/10.1038/s41467-019-14008-1



Supplemental material

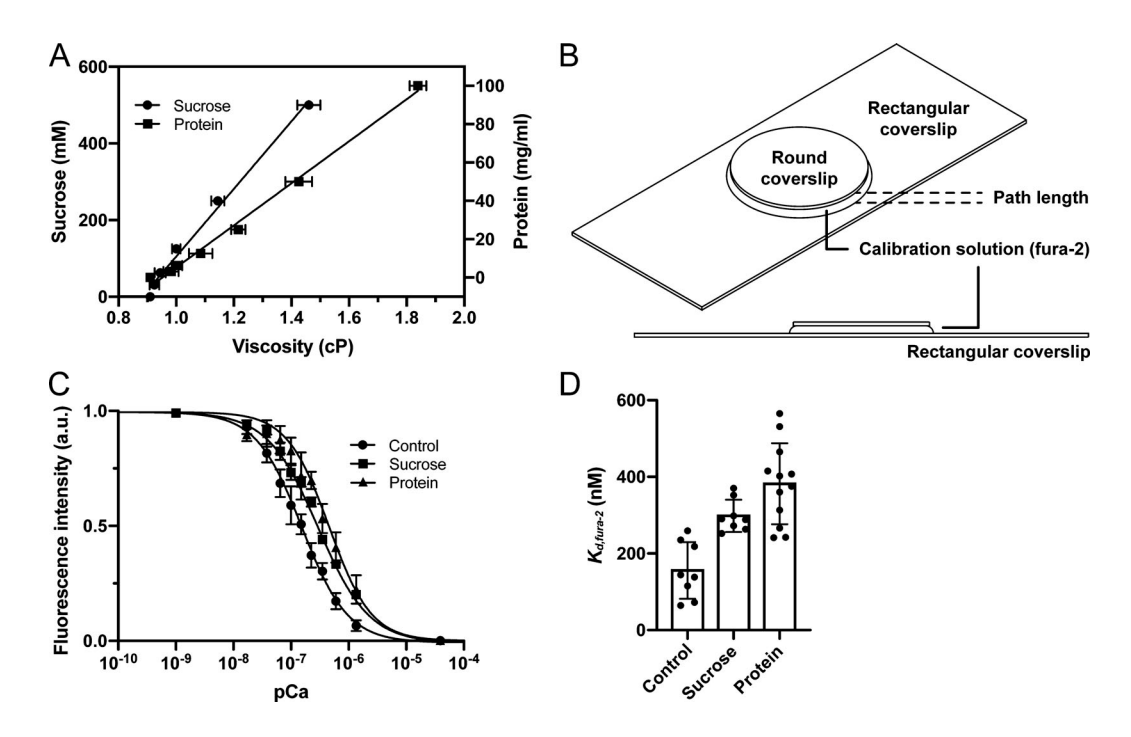


Figure S1. Analyses of fura-2 Ca^{2+} binding affinity in situ. (A) Comparison of the viscosity changes according to the concentration of protein (aldolase) or sucrose. From a linear regression of the measured value, the viscosity of a 20-mg/ml protein-containing solution was equal to that of a 283-mM sucrose-containing solution (dotted line, n = 9). (B) Cartoon showing the condition for the in vitro calibration of fura-2 in the thin layer of solution between the two coverslips. (C) In vitro calibration (fluorescence $[F_{380}]$ -pCa relation) of salt (control), sucrose-containing solution, and protein-containing solution using EGTA-buffered Ca^{2+} calibration solutions. The fluorescence-pCa relation was shifted to the right by 283 mM of sucrose and 20 mg/ml of protein (n = 8, 8, and 12 for control, sucrose, and protein, respectively). (D) Summary of the $K_{d,fura}$ obtained from the fluorescence-pCa relation.

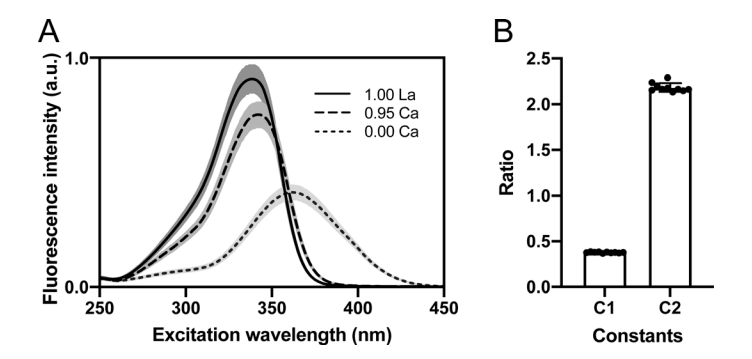


Figure S2. **Calibration factors for in situ calibration of fura-2. (A)** The constants of La³⁺ calibration were used for inhibiting hypercontraction. Gray areas represent SD. The fura-2 fluorescence intensity at 510 nm of emission wavelength according to the excitation wavelength (from 250 to 450 nm) in the cuvette-type spectrophotometer. The La³⁺-fura-2 spectra (black solid line) showed the higher fluorescence intensity at 340 nm, compared with that of 0.95 mM Ca²⁺ spectra (dotted solid line) had the lower fluorescence intensity at 380 nm. **(B)** Summary of the constants (C1 and C2) to correct the fluorescence intensity of La³⁺-fura-2 (see Materials and methods; n = 10).



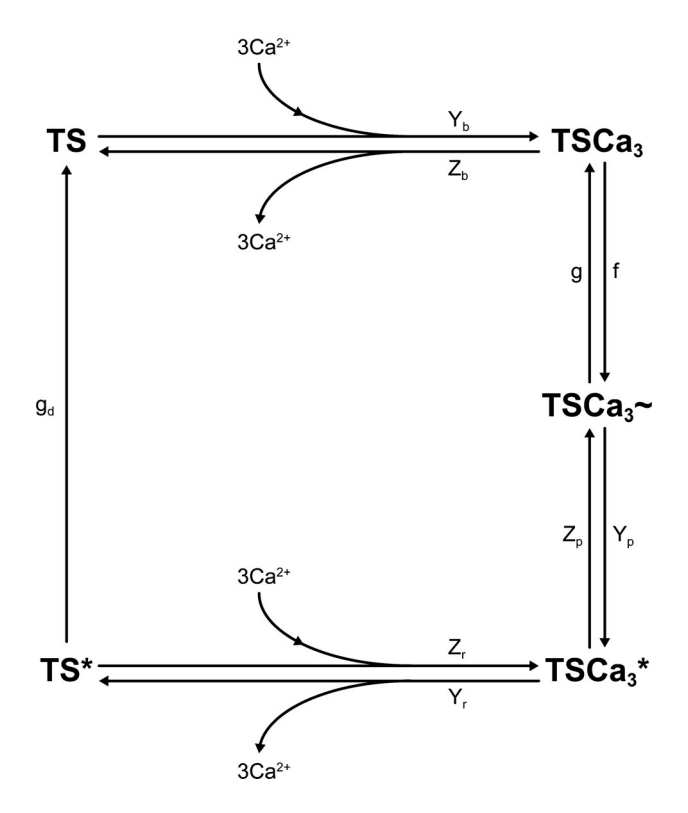


Figure S3. **States of troponin system (TS).** See List of abbreviations for detailed descriptions of each state and kinetic reaction constant.



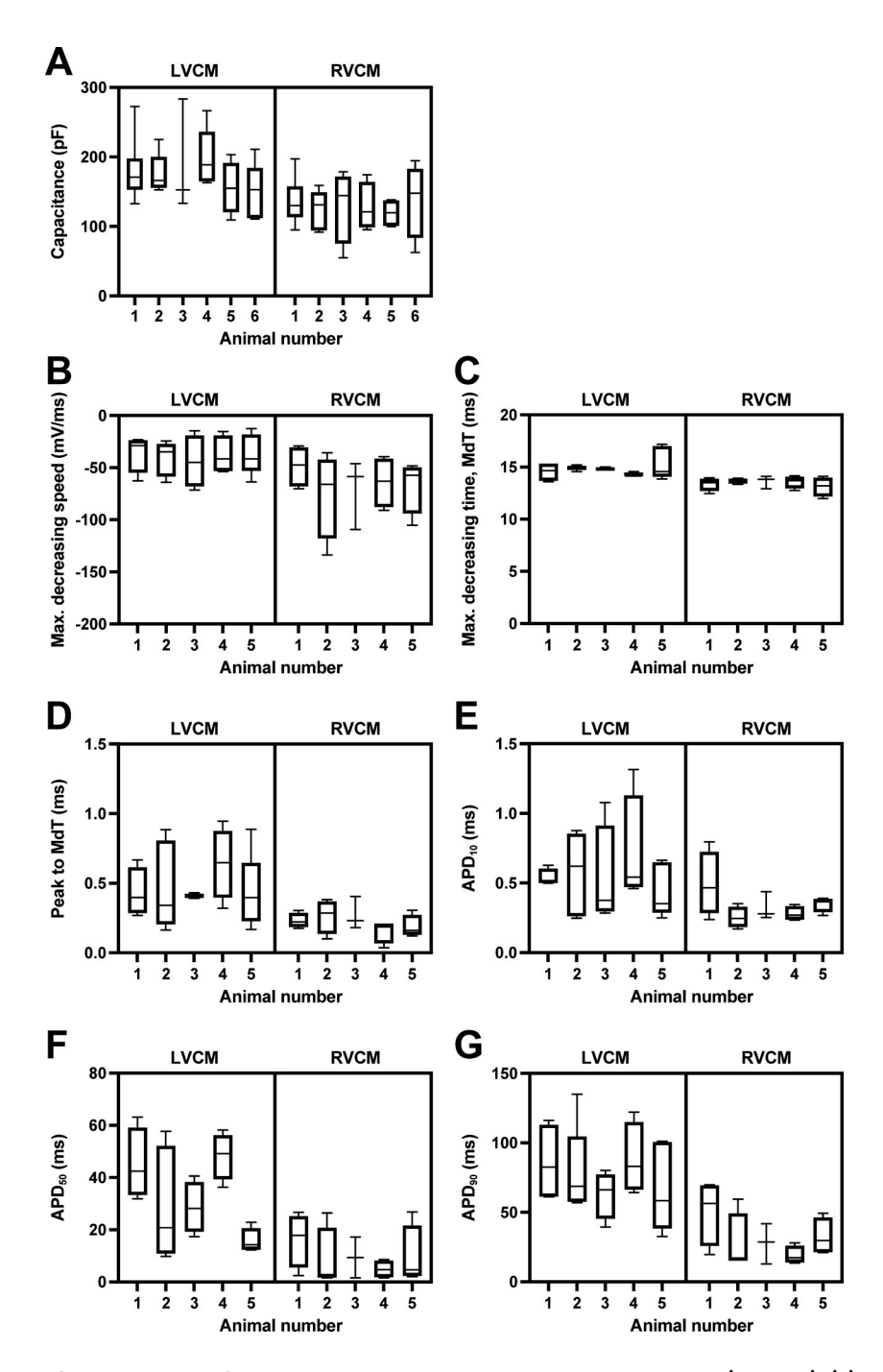


Figure S4. Statistically significant parameters from AP analysis are depicted as box-and-whisker plot (min-max). (A) Capacitance. (B) Maximum decreasing speed. (C) Maximum decreasing time. (D) Peak to maximum decreasing time. (E–G) AP duration. All are significantly different between two ventricles, when tested using nested t test.



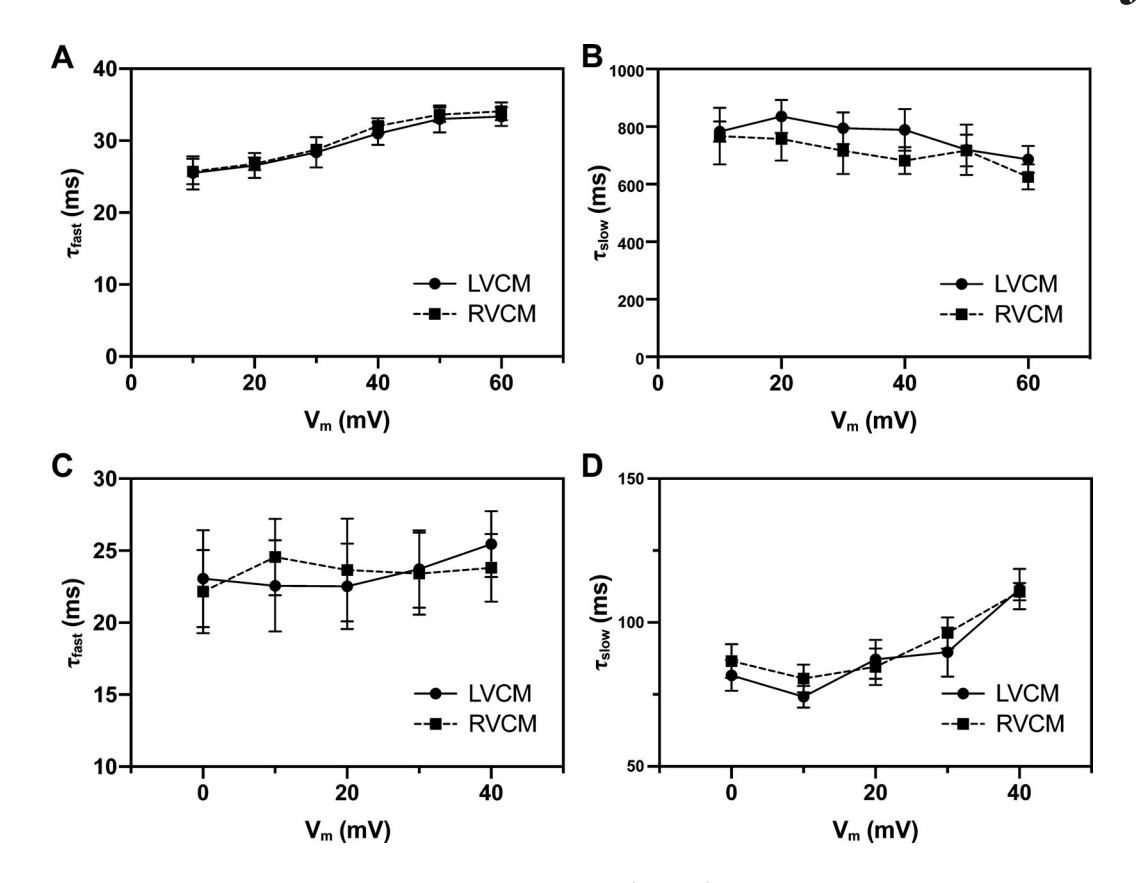


Figure S5. **The speed of** I_{to} **inactivation fitted by a double exponential function. (A and B)** Summary of the fast time constant (τ_{fast} , A) and the slow time constant (τ_{slow} , B) according to the clamp voltage. **(C and D)** The $I_{Co,L}$ inactivation was also fitted by a double exponential function; neither the fast inactivating time constant (τ_{fast} , C) nor the slow inactivating time component (τ_{slow} , D) was different.

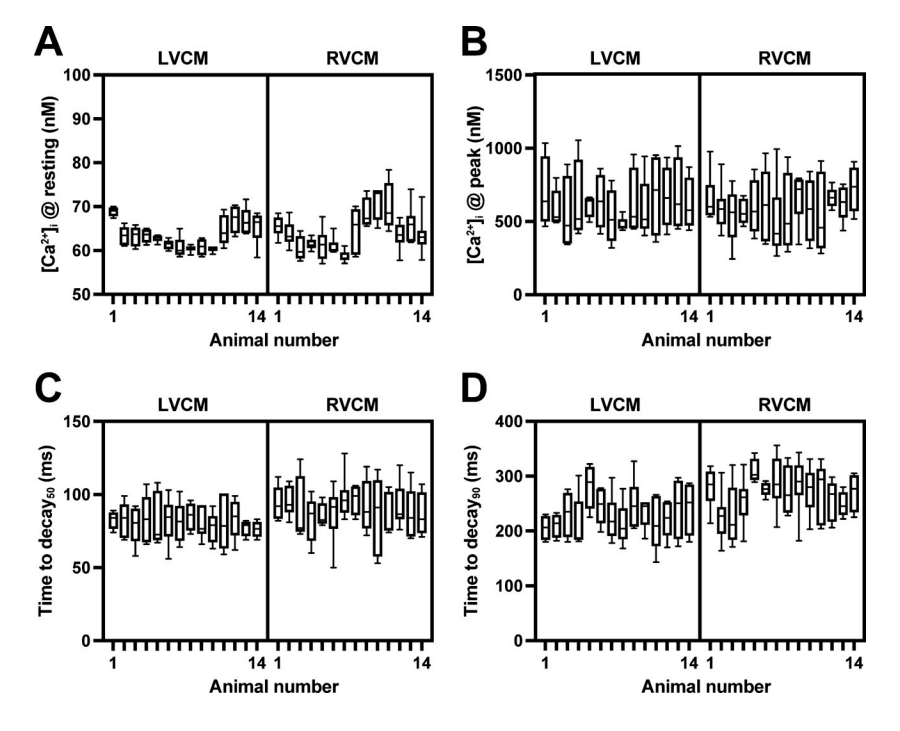


Figure S6. Statistically significant parameters from Ca^{2+} transient analyses are depicted as box-and-whisker plot (min-max). (A–D) Diastolic $[Ca^{2+}]_i$ just before the pulse, the peak level at resting (A), maximum decreasing speed (B), and time to $decay_{50}$ (C) and $decay_{90}$ (D), representing the time from peak to 50 and 90% decay of Ca^{2+} transient, were summarized for each animal.



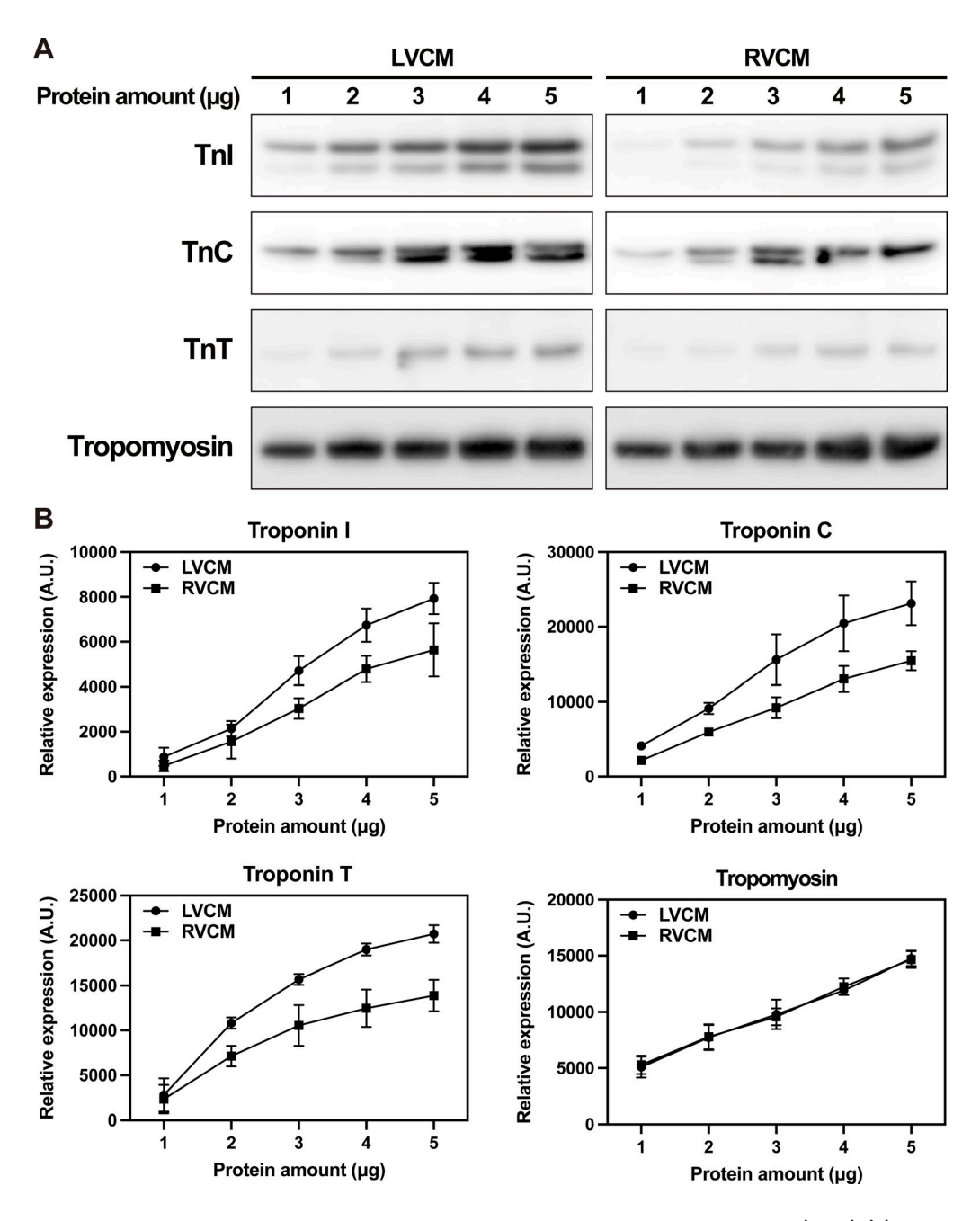


Figure S7. The protein expression of cTn and tropomyosin was measured using quantitative immunoblotting (n = 8). (A) Representative bands are depicted by increasing the total amount of protein loading. (B) The signals of bands, measured and normalized to total protein signal as an internal loading control, are summarized. The expressions of troponin were lower in RVCM at the unsaturated ranges of protein loading, while that of tropomyosin was not different in all ranges.



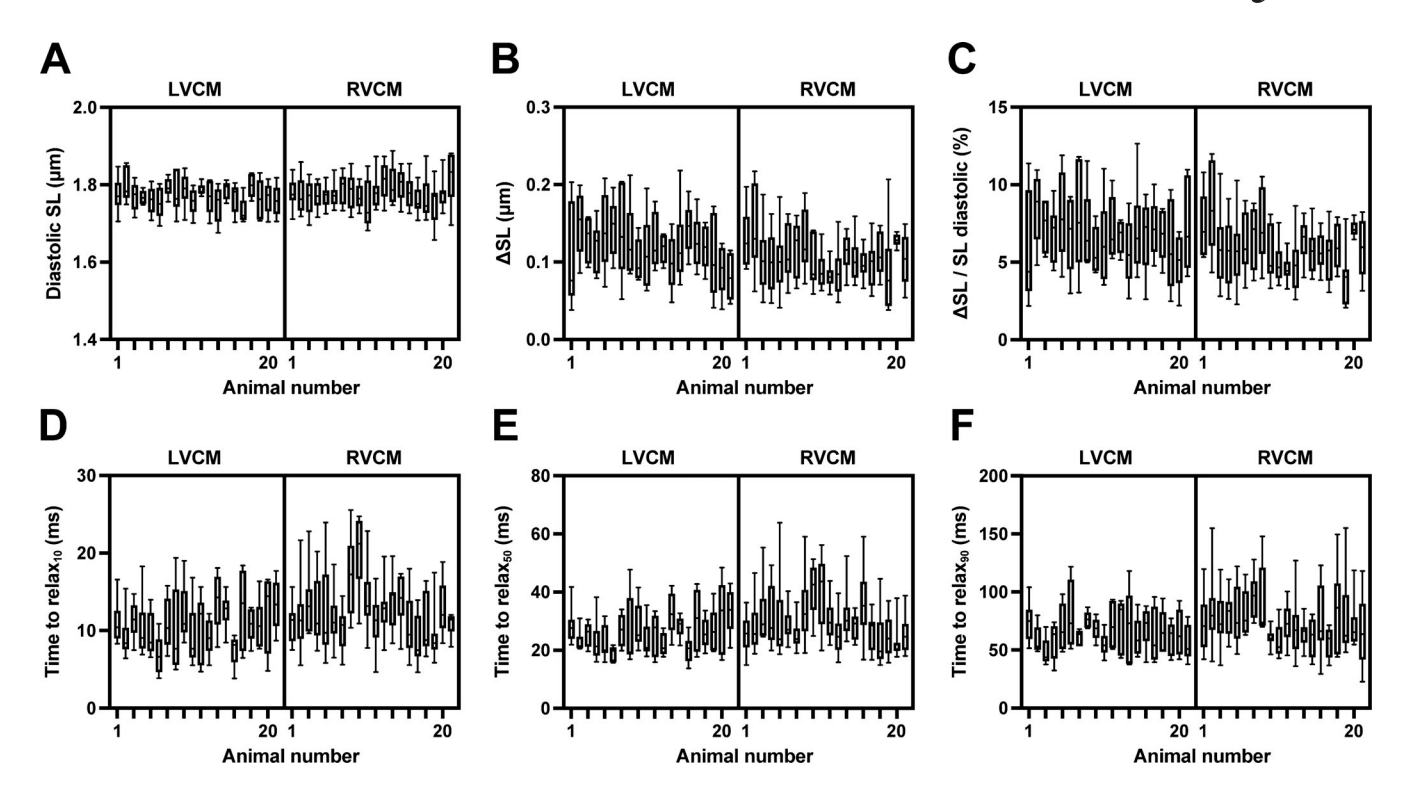


Figure S8. **SL** and its changes (Δ SL) in RVCM and LVCM. (A-C) Summaries comparing the diastolic SL (A), the Δ SL (B), and the percent ratio of Δ SL/diastolic SL in each cell (C). (**D** and **E**) Time to relax₁₀, relax₅₀, and relax₉₀ representing the time from peak to 10, 50, and 90% relaxation of Δ SL, respectively. 20 animals were used for measuring contraction and are depicted individually.



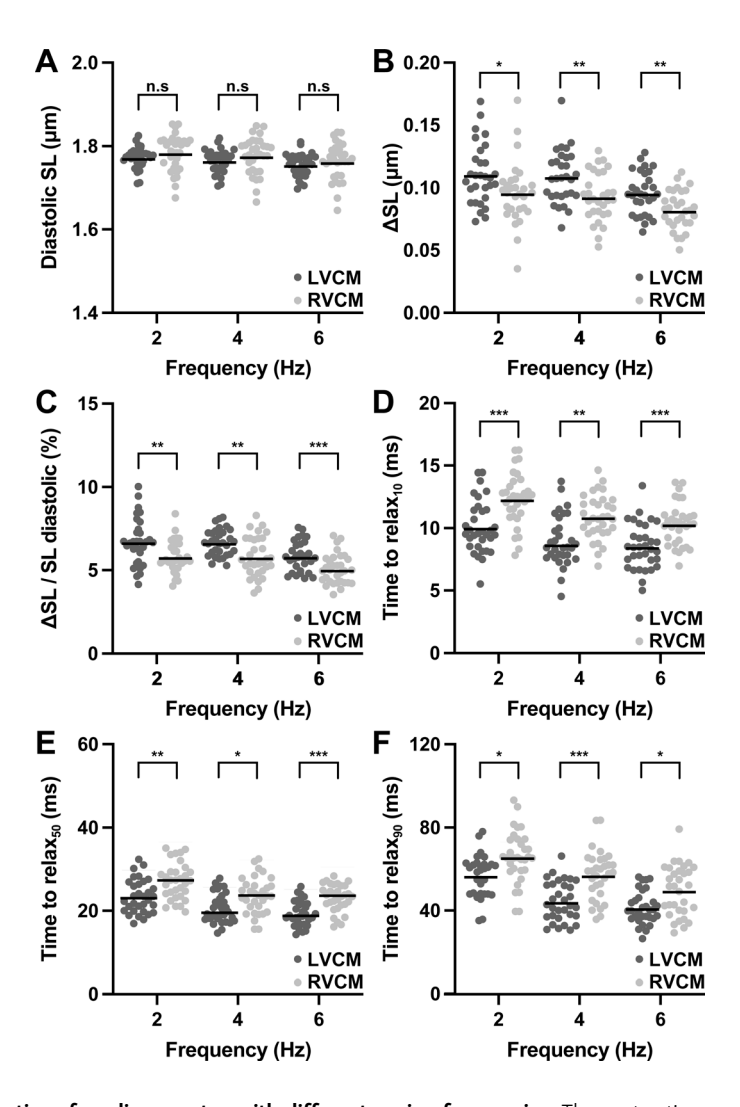


Figure S9. The contractile properties of cardiomyocytes with different pacing frequencies. The contraction was stimulated with three pacing frequencies (2–6 Hz). (A–C) Diastolic SL (A), its changes (Δ SL; B), and the percent ratio of Δ SL/diastolic SL (DC) in LVCM (n=30, n=6) and RVCM (n=30, n=6) are summarized. (D–F) Time from peak to relaxation of Δ SL 10, 50, and 90% is represented as the time to relax₁₀, relax₅₀, and relax₉₀, respectively. All statistical tests performed using nested t test. *, P < 0.05; **, P < 0.01; ***, P < 0.001. The dot means the measured value of individual cells, and the black line in the column means average of measured value.